ปฏิกิริยาการแยกน้ำด้วยตัวเร่งปฏิกิริยาใช้แสงบนไทเทเนียโด้ปด้วยโบรอนและแมกนีเซียม

นางสาว ชุตินันท์ โอรักษ์

วิทยานิพนธ์นี้เป็นส่วนหนึ่งของการศึกษาตามหลักสูตรปริญญาวิศวกรรมศาสตรมหาบัณฑิต
สาขาวิชาวิศวกรรมเคมี   ภาควิชาวิศวกรรมเคมี
คณะวิศวกรรมศาสตร์ จุฬาลงกรณ์มหาวิทยาลัย
ปีการศึกษา 2553

PHOTOCATALYTIC SPLITTING OF WATER OVER TITANIA DOPED WITH B AND Mg

Miss Chutinan Orak

A Thesis Submitted in Partial Fulfillment of the Requirements

for the Degree of Master of Engineering Program in Chemical Engineering

Department of Chemical Engineering

Faculty of Engineering

Chulalongkorn University

Academic Year 2010

Thesis Title	PHOTOCATALYTIC SPLITTING OF WATER OVER TITANIA DOPED WITH B AND Mg
By	Miss Chutinan Orak
Field of Study	Chemical Engineering
Thesis Advisor	Akawat Sirisuk, Ph.D.

Accepted by the Faculty of Engineering, Chulalongkorn University in Partial Fulfillment of the Requirements for the Master's Degree

....Dean of the Faculty of Engineering

(Associate Professor Boonsom Lerdhirunwong, Dr.Ing.)

THESIS COMMITTEE

....Chairman

(Apinan Soottitantawat, Ph.D.)

....Thesis Advisor

(Akawat Sirisuk, Ph.D.)

....Examiner

(Assistant Professor Joongjai Panpranot, Ph.D.)

....External Examiner

(Nattaya Comsup, D.Eng.)

ชุตินันท์   โอรักษ์   : ปฏิกิริยาการแยกน้ำด้วยตัวเร่งปฏิกิริยาใช้แสงบนไทเทเนียโด้ป ด้วยโบรอนและแมกนีเซียม (PHOTOCATALYTIC SPLITTING OF WATER OVER TITANIA DOPED WITH B AND Mg) อ.ที่ปรึกษาวิทยานิพนธ์หลัก: อ. ดร.อัครวัต ศิริสุข, 77 หน้า

งานวิจัยนี้ศึกษาผลของไทเทเนียมไดออกไซด์ถูกโด้ปด้วยโบรอนในปริมาณที่ เหมาะสมเพื่อปรับปรุงประสิทธิภาพในปฏิกิริยาการแยกน้ำในช่วงแสงขาว   ทำการเตรียม ไทเทเนียมไดออกไซด์ถูกเตรียมด้วยวิธีโซล-เจลและเปลี่ยนแปลงปริมาณโบรอนในช่วงร้อยละ 0 ถึง 2 โดยน้ำหนักต่อจากนั้นแมกนีเซียมถูกเติมลงไปในปริมาณร้อยละ 1 โดยน้ำหนัก ตัวเร่ง ปฏิกิริยาถูกเผาที่อุณหภูมิ 350 องศาเซลเซียสเป็นเวลา 2 ชั่วโมง และทำการวิเคราะห์คุณสมบัติ ของตัวเร่งปฏิกิริยาด้วยเครื่องมือต่างๆ เช่น ยูวีวิสดิฟฟิวรีแฟกแตนซ์ เอ็กซ์เรย์ดิแฟรคโตมิเตอร์ การดูดซับไนโตรเจนทางกายภาพ   กล้องจุลทรรศน์อิเล็กตรอนแบบส่องกราด   ฟูเรียทรานส์ ฟอร์มอินฟราเรด และโฟโตลูมิเนสเซนต์ ความว่องไวตัวเร่งปฏิกิริยาในปฏิกิริยาการแยกน้ำถูก วัดภายใต้แสงยูวีและแสงขาว(ความยาวคลื่นมากกว่า   420 นาโนเมตร) เป็นเวลา 5 ชั่วโมง สารละลายที่ใช้ทำปฏิกิริยาเป็นน้ำและเมทานอลในอัตราส่วน 4 ต่อ 1 ประสิทธิภาพการแยก น้ำของไทเทเนียมไดออกไซด์ที่โด้ปด้วยโบรอนและแมกนีเซียมมีค่าเพิ่มขึ้นภายใต้แสงยูวีเมื่อ ปริมาณของโบรอนเพิ่มขึ้นเพราะการดูดซับแสงในช่วงแสงขาวที่ดีขึ้นและการกลับมารวมตัว กันของอิเล็กตรอนกับโฮลได้ช้าลง   เมื่อทำปฏิกิริยาการแยกน้ำภายใต้แสงขาวตัวเร่งปฏิกิริยาที่ ประกอบด้วยโบรอนร้อยละ 1 และ แมกนีเซียมร้อยละ 1 โดยน้ำหนัก จะได้ความว่องไวในการ เกิดปฏิกิริยาสูงที่สุดซึ่งเป็นผลมาจากบทบาทของเซ็นซิไตเซอร์ที่มีผลต่อการแยกน้ำในแสงขาว

ภาควิชา ......วิศวกรรมเคมี.........   ลายมือชื่อนิสิต..........ชุตินันท์ โอรักษ์
สาขาวิชา .....วิศวกรรมเคมี.........   ลายมือชื่อ อ.ที่ปรึกษาวิทยานิพนธ์หลัก.........
ปีการศึกษา .....2553...............

##5270273021: MAJOR CHEMICAL ENGINEERING

KEY WORDS: TITANIUM DIOXIDE/ PHOTOCATALYTIC ACTIVITY FOR WATER SPLITTING/ VISIBLE REGION.

CHUTINAN ORAK: PHOTOCATALYTIC SPLITTING OF WATER OVER TITANIA DOPED WITH B AND Mg. ADVISOR: AKAWAT SIRISUK, Ph.D, 77 pp.

Titanium dioxide was doped with boron in order to improve its photocatalytic activity for water splitting in the visible light region. Titania was synthesized via a sol-gel method and boron was added to the sol in the amount ranging from 0 to 2%(w/w). Then magnesium was added to the boron-doped titania in the amount of 1%(w/w). The catalysts were fired at 350 °C for two hours. The catalysts were characterized by UV-visible diffuse reflectance spectroscopy, X-ray diffractometry, nitrogen physisorption, scanning electron microscopy, fourier transform Infrared (FT-IR), and photoluminescence. The photocatalytic activities of boron-doped catalysts were evaluated for the splitting of water under both ultraviolet light and visible light (wavelength > 420 nm) irradiations for the duration of five hours. Methanol was added to act as a sacrificial agent at the volume ratio of water to methanol of 4 to 1. The photocatalytic activity of co-doped TiO_2 increased under UV irradiation as the boron loading increased because of better absorption in the visible region and slower recombination of photogenerated charge carriers. Under visible irradiation, the highest photocatalytic activity was obtained by the catalyst that contained 1% (w/w) B and 1% (w/w) Mg. This was attributed to the role of carbonaceous species sensitizer as a visible light.

Department : Chemical Engineering   Student's Signature Chutinan Orak

Field of Study : Chemical Engineering   Advisor's Signature

Academic Year : 2010

ACKNOWLEDGEMENTS

CONTENTS

LIST OF TABLES

LIST OF FIGURES

CHAPTER I

INTRODUCTION

Hydrogen is considered as an idea fuel for the future. Hydrogen fuel can be produced from clean and renewable energy sources and, thus, its life cycle is clean and renewable. Solar and wind are the two major sources of renewable energy and they are also the promising sources for renewable hydrogen production. However, presently, renewable energy contributes only about 5% of the commercial hydrogen production primarily via water electrolysis, while other 95% hydrogen is mainly derived from fossil fuels.

Water splitting using photocatalysts is not a new theme. Water splitting has been studied in the research fields of catalysis, electrochemistry, photochemistry, organic and inorganic chemistry, etc. for about 30 years since the Honda–Fujishima effect was reported using a TiO_2 semiconductor electrode. However, the number of reported photocatalysts which were able to decompose water into H_2 and O_2 in a stoichiometric amount with a reasonable activity had been much limited. The active photocatalysts are only oxide materials at the present stage. In such a background, various types of new photocatalysts for water splitting have been developed (Kudo, 2006).

For the purpose of the goals of improving optical absorption and photocatalytic activity, all kinds of attempts have been made to extend the light absorption toward the visible light range and to prohibit the recombination of electron–hole pairs. Based on the previous researches reported in the literature, loading noble metal over semiconductor photocatalyst, doping of titania with transition metal, doping of titania with rare earth metal , treating of titania with hydrogen peroxide, photosensitizing titania, and compounding titania with other

materials have been investigated to raise photocatalytic performance (Ling et al., 2008).

Titanium dioxide in photocatalytic water splitting technology has great potential for low-cost, environmentally friendly, solar production of hydrogen to support the future hydrogen economy. Presently, the solar-to-hydrogen energy conversion efficiency is too low for the technology to be economically sound. The main barriers are the rapid recombination of photo-generated electron/hole pairs as well as backward reaction and the poor activation of titanium dioxide by visible light. In response to these deficiencies, many investigators have been conducting research with an emphasis on effective remediation methods. Some investigators studied the effects of addition of sacrificial reagents and carbonate salts to prohibit rapid recombination of electron/hole pairs and backward reactions. Other research focused on the enhancement of photocatalysis by modification of titanium dioxide by means of metal loading, metal ion doping, dye sensitization, composite semiconductor, anion doping, and metal ion implantation (Eakachai, 2007).

The photo-excited electrons can be transferred from the conduction band of titanium dioxide to metal particles deposited on the surface of titanium dioxide, while the photo-generated holes in the valence band remain on the titanium dioxide. These activities greatly reduce the possibility of electron-hole recombination, resulting in efficient separation of charge carriers and better photocatalytic reactions. In this work, we synthesized titanium dioxide via a sol-gel method and loaded a combination of two metals, i.e., boron together with either magnesium. The catalysts were employed in photocatalytic spitting of water.

A number of methods have been used to prepare TiO_2 nanoparticle, such as chemical precipitation, micro emulsion, hydrothermal crystallization and sol–gel. Sol–gel is one of the most successful techniques for preparing nanosized metallic oxide materials with high photocatalytic activities. By tailoring the chemical structure of primary precursor and carefully controlling the processing variables,

nanocrystalline products with very high level of chemical purity can be achieved (Su et al., 2004).

In this study, TiO_2 photocatalyst is doped with boron and magnesium oxide at various concentrations. The activity in photocatalytic water splitting under UV light and visible lights are compared.

To improve the performance of TiO_2 in photocatalytic water splitting under visible light by doping with boron and magnesium.

The objective of the research is to investigate the doing of TiO_2 using two types of metals for use in photocatalytic splitting of water

The present study is arranged as follows:

Chapter I is the introduction.

Chapter II describes the basic information about titanium dioxide, a sol-gel process, and photocatalytic splitting of water.

Chapter III presents literature survey of the previous works related to this research.

Chapter IV describes preparation procedures for the catalyst, characterization techniques employed, and the experimental setup.

Chapter V presents the experimental results and discussion.

ChapterVI includes the overall conclusions of this research and recommendation for future works.

CHAPTER II

THEORY

2.1 Physical and chemical properties of titanium dioxide

Titanium dioxide may take on any of the following three crystal structures:

Anatase generally exhibits a higher photocatalytic activity than other types of titanium dioxide. The three forms of titanium (IV) oxide have been prepared in laboratories but only rutile, the thermally stable form, has been obtained in the form of transparent large single crytal. The transformation from anatase to rutile is accompanied by the evolution of ca. 12.6 kJ/mol (3.01 kcal/mol), but the rate of transformation is greatly affected by temperature and the presence of other substances, which may either catalyze or inhibit the reaction. The lowest temperature at which transformation from anatase to rutile takes place at a measurable rate is around 700º C, but this is not a transition temperature. The change is not reversible since ΔG for the change from anatase to rutile is always negative.

Brookite has been produced by heating amorphous titanium (IV) oxide, which is prepared from an alkyl titanate or sodium titanate, with sodium or potassium hydroxide in an autoclave at 200 to 600ºC for several days. The important commercial forms of titanium (IV) oxide are anatase and rutile, and they can readily be distinguished by X-ray diffractometry.

Rutile, which tends to be more stable at high temperature and thus is sometimes found in igneous rocks, anatase, which tends to be more stable at lower temperatures (both belonging to the tetragonal crystal system), and brookite, which is usually found only in minerals and has a structure belonging to the orthorhombic crystal system. The titanium dioxide use in industrial products, such as paint, is almost a rutile type. These crystals are substantially pure titanium dioxide but usually amount of impurities, e.g., boron, Magnesium or calcium, which darken them. A summary of crystallographic properties of the three varieties is given in Table 2.1

Table 2.1 Crystallographic properties of anatase, brookite, and rutile.

Properties	Anatase	Brookite	Rutile
Crystal structure	Tetragonal	Orthorhombic	Tetragonal
Optical	Uniaxial, Negative	Biaxial, positive	Uniaxial, Negative
Density, g/cm3	3.9	4.0	4.23
Harness, Mohs scale	$5\frac{1}{2}$ - 6	$5\frac{1}{2}$ - 6	$7 - 7\frac{1}{2}$
Unit cell	$D_4a^{19} . 4TiO_2$	$D_2h^{15} . 8TiO_2$	$D_4h^{12} . 3TiO_2$
Dimension, nm			
a	0.3758	0.9166	0.4584
b		0.5436	
c	0.9514	0.5135	2.953

The three allotropic forms of titanium dioxide have been prepared artificially but only rutile, the thermally stable form, has been obtained in the form of transparent large single crystal. The transformation form anatase to rutile is accompanied by the evolution of ca. 12.6 kJ/mol (3.01 kcal/mol), but the rate of transformation is greatly affected by temperature and by the presence of other substance which may either catalyze of inhibit the reaction. The lowest temperature at which conversion of anatase to rutile takes place at a measurable rate is ca. 700ºC, but this is not a transition temperature. The change is not reversible; ΔG for the change from anatase to rutile is always negative.
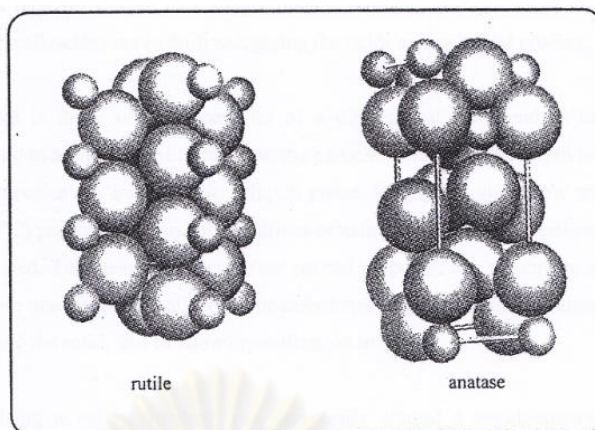
Figure 2.1 Crystal structures of Titanium dioxide in rutile, and anatase

Although anatase and rutile are both tetragonal, they are not isomorphous (see Figure 2.1). The two tetragonal crystal types are more common because they are easy to make. Anatase occurs usually in near-regular octahedral, and rutile forms slender prismatic crystal, which are frequently twinned. Rutile is the thermally stable form and is one of the two most important ores of titanium.

Since both anatase and rutile are tetragonal, they are both anisotropic, and their physical properties, e.g. refractive index, vary according to the direction relative to the crystal axes. In most applications of these substances, the distinction between crystallographic directions is lost because of the random orientation of large numbers of small particles, and it is mean value of the property that is significant.

2.2 Preparation of Titanium dioxide via a sol-gel method

In sol–gel processes, TiO_2 is usually prepared by the reactions of hydrolysis and polycondensation of titanium alkoxides, $Ti(OR)_n$ to form oxopolymers, which are then transformed into an oxide network. The reaction scheme is usually written as follows:

Hydrolysis:

$$M(OR)_n + H_2O \rightarrow M(OR)_{n-1}(OH) + ROH \qquad (2.1)$$
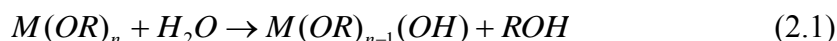
Condensation Dehydration:

$$M(OR)_n + M(OR)_{n-1}(OH) \rightarrow M_2O(OR)_{2n-2} + ROH \qquad (2.2)$$

Dealcoholation:

$$2M(OR)_{n-1}(OH) \rightarrow M_2O(OR)_{2n-2} + H_2O \qquad (2.3)$$
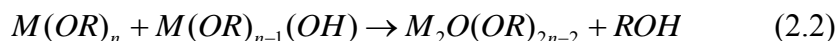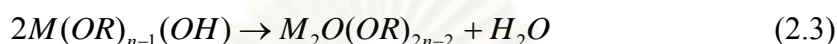
The overall reaction is

$$M(OR)_n + \frac{n}{2}H_2O \rightarrow MO_{n/2} + nROH \qquad (2.4)$$
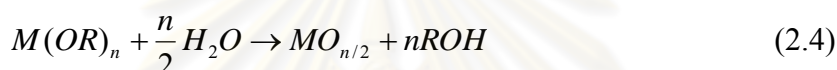
A typical example of a sol-gel method is the addition of metal alkoxides to water. The alkoxides are hydrolyzed, giving the oxide as a colloidal product.

Sol is made of solid particles of a diameter of few hundred nanometers suspending in a liquid phase. After that, the particles condense into gel, in which solid macromolecules are immersed in a liquid phase. Drying the gel at low temperature (25-100ºC) produces porous solid matrices or xerogels. To obtain a final product, the gel is heated. This heat treatment serves several purposes, i.e., to remove solvent, to decompose anion such as alkoxides or carbonates to give oxides, to rearrange of the structure of the solid, and to allow crystallization to occur.

Using a sol-gel method, one can easily control a stoichiometry of solid solution and homogeneous distribution of nanoparticles and metal oxides. In addition, the metal oxides can be prepared easily at room temperature and high purity can be obtained.

2.3 Mechanisms of semiconductor photocatalytic water-splitting or hydrogen production

The electronic structure of a semiconductor plays a key role in semiconductor photocatalysis. Unlike a conductor, a semiconductor consists of VB and CB. Energy difference between these two levels is said to be the band gap (E_g). Without excitation, both the electrons and holes are in valence band. When semiconductors are excited by photons with energy equal to or higher than their band gap energy level, electrons receive energy from the photons and are thus promoted from VB to CB if the energy gain is higher than the band gap energy level. For semiconductor TiO_2, the reaction is expressed as:

$$TiO_2 \xrightarrow{hv} e^-_{TiO_2} + h^+_{TiO_2} \qquad (2.5)$$

The photo-generated electrons and holes can recombine in bulk or on surface of the semiconductor within a very short time, releasing energy in the form of heat or photons. Electrons and holes that migrate to the surface of the semiconductor without recombination can reduce and oxidize the reactants adsorbed by the semiconductor, respectively. The reduction and oxidation reactions are the basic mechanisms of photocatalytic hydrogen production and photocatalytic water/air purification, respectively. Both surface adsorption as well as photocatalytic reactions can be enhanced by nano-sized semiconductors as more reactive surface area is available.

For hydrogen production, the CB level should be more negative than hydrogen production level ($E_{H2=H2O}$) while the VB should be more positive than water oxidation level ($E_{O2=H2O}$) for efficient oxygen production from water by photocatalysis. The photocatalytic hydrogen production by TiO_2 is shown in Figure 2.2.
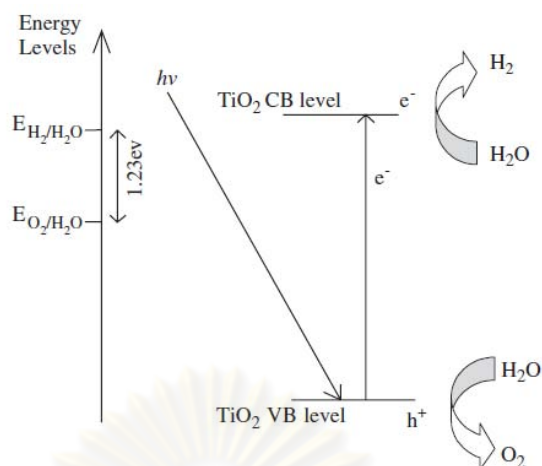
Figure 2.2 Mechanism of TiO_2 photocatalytic water-splitting for hydrogen production

Theoretically, all types of semiconductors that satisfy the above-mentioned requirements can be used as photocatalysts for hydrogen production. However, most of the semiconductors, such as CdS and SiC, that cause photo corrosion, are not suitable for water-splitting. Having strong catalytic activity, high chemical stability and long lifetime of electron/hole pairs, TiO_2 is the most widely used photocatalyst. Presently, the energy conversion efficiency from solar to hydrogen by TiO_2 photocatalytic water-splitting is still low, mainly due to the following reasons:

(1) Recombination of photo-generated electron/hole pairs: CB electrons can recombine with VB holes very quickly and release energy in the form of unproductive heat or photons.

(2) Fast backward reaction: Decomposition of water into hydrogen and oxygen is an energy increasing process, thus backward reaction (recombination of hydrogen and oxygen into water) easily proceeds.

(3) Inability to utilize visible light: The band gap of TiO_2 is about 3.2 eV and only UV light can be utilized for hydrogen production. Since the UV light only accounts for about 4% of the solar radiation energy while the visible light contributes about 50%, the inability to utilize visible light limits the efficiency of solar photocatalytic hydrogen production.

2.4 Roles of metal in hydrogen production from photocatalytic water splitting over titanium dioxide

Transitional metal ion doping and rare earth metal ion doping have been extensively investigated for enhancing the TiO_2 photocatalytic activities. Meng and coworker (2007) found that doping of metal ions could expand the photo-response of TiO_2 into visible spectrum. As metal ions are incorporated into the TiO_2 lattice, impurity energy levels in the band gap of TiO_2 are formed, as indicated below:

$$M^{n+} + hv \rightarrow M^{(n+1)+} + e_{ch}^{-} \qquad (2.6)$$

$$M^{n+} + hv \rightarrow M^{(n-1)+} + h_{vb}^{-} \qquad (2.7)$$

where M and M^{n+} represent metal and the metal ion dopant, respectively. Furthermore, electron (hole) transfer between metal ions and TiO_2 can alter electron hole recombination as:

$$\text{Electron trap}: M^{n+} + e_{cb}^{-} \rightarrow M^{(n-1)+} \qquad (2.8)$$

$$\text{Hole trap}: \quad M^{n+} + h_{vb}^{+} \rightarrow M^{(n-1)-} \qquad (2.9)$$
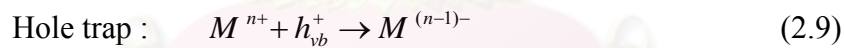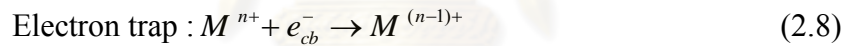
The energy level of $M^{n+}/M^{(n-1)+}$ should be less negative than that of the CB edge of TiO_2, while the energy level of $M^{n+}/M^{(n-1)+}$ should be less positive than that of the VB edge of TiO_2. For photocatalytic reactions, carrier transferring is as important as carrier trapping. Only if the trapped electron and hole are transferred to the surface, photocatalytic reactions can occur. Therefore, metal ions should be doped near the surface of TiO_2 particles for a better charge transferring. In case of deep doping, metal ions likely behave as recombination centers, since electron/hole transferring to the interface is more difficult.

CHAPTER III

LITERATURE REVIEWS

Titanium dioxide is one of the most promising photocatalyst because of its high efficiency, low cost, chemical inertness, and long-term stability. It has been used in various fields, such as solar cells, photocatalytic splitting of water for green-energy hydrogen production, selective synthesis of organic compounds, air purification, removal of organic and inorganic pollutants, and photo killing of pathogenic organisms (Grabowska et al., 2009).

TiO_2 is a good photocatalyst due to its stability and high activity. However, its band gap is so large (E_g = 3.20 eV) to be only excited by ultraviolet light with a wavelength of no longer than 387.5 nm, which accounts for only 4% of the incoming solar energy. Thus, it is significant to develop visible-light driven photocatalyst with high activity. To make the best use of solar energy, there have been many studies on doped TiO_2. Among them metal ion doping has extensively been studied, for example, transition-metal ions, rare-earth ions (Yuexiang et al., 2008).

3.1 Photocatalytic decomposition of water to hydrogen on titanium dioxide

For H_2 production from water, many studies have concluded that direct photodecomposition of water into H_2 and O_2 has a very low efficiency due to rapid reverse reaction. A much higher hydrogen production rate can be obtained by addition of a sacrificial reagent, such as alcohols, carbohydrates solid carbon, sulfide, etc. which is oxidized to a product that is less reactive toward hydrogen (Wu et al., 2004). This suggests that photoexcited electrons and holes can be efficiently separated in a small semiconductor particle and that they are available for an irreversible chemical reaction, oxidization of sacrificial reagent. It is, therefore, inferred that a low efficiency of photodecomposition of water into H_2 and O_2 is mainly due to a rapid reverse reaction between produced H_2 and O_2. Thus, a critical problem to be resolved

for realizing the up-hill reaction efficiently is how to prevent such thermodynamically favored reverse reaction (Moon et al., 2000).

Of particular interest in these intercalated nanoparticles was the production of hydrogen from water containing a sacrificial agent under visible light irradiation with quantum yields as 10%. This might be attributable to the ease in donating lone-pair electrons to the valence band hole upon the photocatalyst excitation. Compared to other types of sacrificial reagents among the alcohol series itself, methanol was found to be the most effective and strongest sacrificial reagent to yield the highest photocatalytic H_2 evolution activity.

For hydrogen production from a water/methanol solution, depending on reaction conditions and on whether metal catalyst used, the reaction could proceed either stepwise, involving stable intermediates, as suggested by Sakata and coworker (1982) :

$$MeOH(l) \xleftrightarrow{hv,catalyst} HCHO(g) + H_2(g) \qquad (3.1)$$

$$HCHO(g) + H_2O(l) \xleftrightarrow{hv,catalyst} HCO_2H(l) + H_2(g) \qquad (3.2)$$

$$HCO_2H(l) \xleftrightarrow{hv,catalyst} CO_2(g) + H_2(g) \qquad (3.3)$$
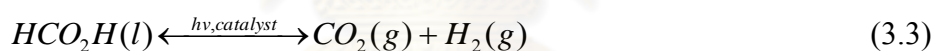
Or in step reaction on catalyst surface to give the overall reaction, as suggested by Chen and coworkers (1998) :

$$MeOH(l) + H_2O(l) \xleftrightarrow{hv,catalyst} CO_2(g) + 3H_2(g) \qquad (3.4)$$
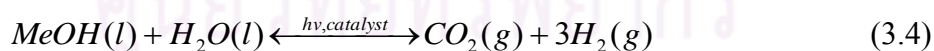
3.2 Roles of metals on titanium dioxide in photocatalytic reaction

The basic principles of heterogeneous photocatalysis can be summarized shortly as follows. A semiconductor (SC) is characterized by an electronic band structure in which the highest occupied energy band, called valence band (VB), and the lowest empty band, called conduction band (CB), are separated by a band gap, i.e. a region of forbidden energies in a perfect crystal. When a photon of energy higher or

equal to the band gap energy is absorbed by a semiconductor particle, an electron from the VB is promoted to the CB with simultaneous generation of a hole (h^+) in the VB. The e_{cb}^- and the h_{vb}^+ can recombine on the surface or in the bulk of the particle in a few nanoseconds (and the energy dissipated as heat) or can be trapped in surface states where they can react with donor (D) or acceptor (A) species adsorbed or close to the surface of the particle. Thereby, subsequent anodic and cathodic redox reactions can be initiated (Figure. 3.1) (Marta, 1999).
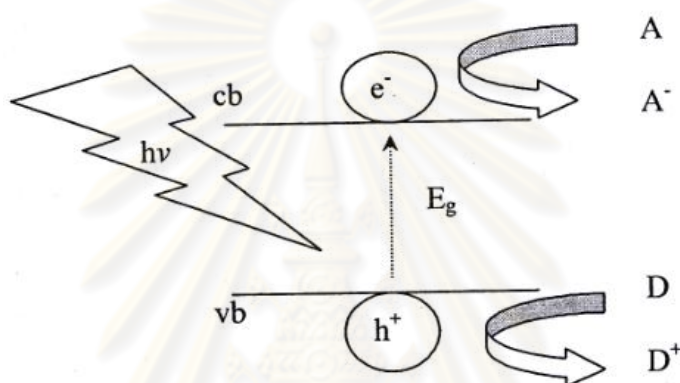
Figure 3.1 Simplified diagram of the heterogeneous photocatalytic processes occurring on an illuminated semiconductor particle.

3.3 Effective of boron doped titanium dioxide

To improve the photocatalytic reactivity of TiO_2 and to extent its light absorption into the visible region several approaches have been proposed, such as metal-ion or non-metal doped TiO_2. TiO_2 doped with boron was prepared by several authors, which reported enhancing photocatalytic activity under UV or visible light in degradation of pollutant. Hence, boron as co-doping was suitable for splitting of water under UV and visible region.

Qincai and coworkers (2008) refered that based on the previous researches reported in the literature, the doping metal atoms present individual phases dispersed into TiO_2, trapping temporarily the photogenerated charge carriers and inhibiting the recombination of photoinduced electron–hole pairs when the electron–hole pairs migrate from the inside of the photocatalyst to the surface.

Yuexiang and coworkers (2008) refered that B-doped TiO_2 showed high photocatalytic activity compared to pure TiO_2 under UV light irradiation. The type of B-doping into TiO_2 strongly depends on the preparation method (synthesis route precursors, and calcination conditions). While Chen et al. observed a band gap increase due to B-doping, attributed to quantum-size effect, Zhao and coworkers (2007) measured a red shift. The apparent contradiction can be explained considering the different geometry and electronic structures of the B-doped TiO_2. And they prepared visible-light boron and nitrogen co-doped titania (B–N–TiO_2) photocatalyst by sol–gel method with titanium tetra-n-butyl oxide, urea and boric acid as precursors. A part of doping boron enters into titania lattice and most of the boron exists at the surface of the catalyst. The crystallite size of B–N–TiO_2 decreases compared to N–TiO_2, while its photocurrent and the surface hydroxyl group increase. Furthermore, doping boron could act as shallow traps for photoinduced electrons to prolong the life of the electrons and holes. Therefore, the visible-light activity of B–N–TiO_2 increases greatly compared with that of N–TiO_2.

Na and coworkers (2008) studied the boron-doped TiO_2 nanotube arrays were fabricated by potentiostatic anodization of titanium in an aqueous electrolyte containing fluoride ion and sodium fluoroborate ($NaBF_4$). Red shifts and enhanced absorption intensities in both UV and visible light regions are observed in the spectra of UV‑vis absorption of B-doped samples. The B-doped nanotube arrays show

improved photochemical capability under both simulated sunlight and UV irradiation. The visible photoelectrocatalytic (PEC) activities of the prepared electrodes were evaluated using atrazine as a test substance under simulated sunlight irradiation. The kinetic constant of PEC degradation of atrazine using B-doped electrode with 3.1 at.% of boron is 53% higher than that using non-doped one. A synergetic effect of the photocatalytic (PC) and electrochemical (EC) processes is observed.

Yaling and coworkers (2008) prepared TiO_2 nanotubes electrode in $C_2H_2O_4 \cdot 2H_2O+NH_4F$ electrolyte by electrochemical anodization. $C_2H_2O_4 \cdot 2H_2O$ was ever used to fabricate nanoporous anodic aluminum oxide by electrochemical anodization. Diffuse reflectance absorption spectra (DRS) analysis indicated that B-doped samples displayed stronger absorption in both UV and visible range. B-doped TiO_2 nanotubes electrode annealed at 700ºC through CVD showed higher photoelectroncatalytic (PEC) efficiency in methyl orange (MO) degradation than that annealed at 400ºC and 550ºC. MO degradation was substantially enhanced with the increasing applied bias potential. Moreover, there was a synergetic effect between the electrochemical and photocatalytic processes, and the synergetic factor R reached 1.45. B-doped TiO_2 nanotubes electrode showed good stability after 10 times by repeating photoelectrocatalysis of MO.

Grabowska and coworkers (2009) prepared boron-doped TiO_2 by the sol-gel method and by grinding TiO_2 powder with a boron compounds (boric acid and boric acid triethyl ester followed by calcinations at temperature range 200 to 600ºC. The photocatalytic activity of obtained powders in visible light was estimated by measuring the decomposition rate of phenol (0.21mmol/dm^3) in an aqueous solution. The best photoactivity under visible light was observed for B-TiO_2 modified with 2 wt% of boron prepared by grinding ST-01 with dopant followed by calcinations at 400ºC. This photocatalyst contains 16.9 at.% of carbon and 6.6 at.% of boron in surface layer and its surface area is 192 m^2/g.

Romana and coworkers (2008) recommended about boron, however, has not been investigated as extensively as other main group dopants, and thus the exact role of boron as a dopant remains controversial. Some argue that boron-doping into TiO_2 results in a red shift for the UV absorption band to the visible region. The rationalization is that the impurity states newly introduced by boron-doping overlap

sufficiently with the 2p electronic states of oxygen. Yet, others hold the opposite to be true by reporting that boron incorporation into TiO_2 results in a blue shift (rather than a red shift) due to a decrease in the crystal size (quantization effect). Thus the exact role of boron on optical absorbance and photocatalytic activity of TiO_2 awaits further investigations. In contrast to this controversy concerning the role of boron, unanimous agreement is that transition metals narrow the bandgap and at the same time reduce the recombination rate of photogenerated electrons and holes.

3.4 Effective of magnesium doped titanium dioxide

In order to slow down the recombination rate of electron-hole pairs and to utilize visible light, researches have modified TiO_2 particles by selective surface treatments, such as doping metal ions on TiO_2. There have been many reports on transition metal, rare earth and noble metal ion doping of TiO_2, but studies on alkaline-earth metal ion co-doping with metalloid as boron of TiO_2 and their photocatalytic properties have never been reported. Mg doping on TiO_2 acts as a charge recombination and electron trap sites leading to better charge separation which results in higher photocatalytic activity.

Bandara and coworkers (2004) prepared a new bilayer TiO_2/MgO nanoporous catalyst was fabricated in which the thin layer of insulating MgO on TiO_2 acts as electron trap and barrier for recombination, enhancing the overall photocatalytic activity of TiO_2. The photocatalytic activity of MgO coated TiO_2 has been studied for the oxidation of 2-chlorophenol, 2,4-dichlorophenol (2,4-DCP) and 4-aminobenzoic acid in aqueous solution. It has been shown that the coating of thin layer of MgO particles on TiO_2 particles enhances the photocatalytic activity of the composite system for the oxidationof chlorophenols and aminobenzoic acid in aqueous solution. The photocatalytic activity enhancement originated as a result of trapping of photogenerated electron on MgO defect sites and holes on TiO_2 particles, allowing wider charge separation and lesser recombination.

Venkatachalam and coworkers (2007) synthesized magnesium and barium doped TiO_2 nanoparticles by sol–gel method. The pure TiO_2 nanoparticles contained both anatase and rutile phases together, but Mg^{2+} or Ba^{2+} metal ion doped nano TiO_2

gave only anatase phase. The photocatalytic degradation of 4-Chlorophenol (4-CP) over nanosize TiO_2 and Mg^{2+} and Ba^{2+} doped nano TiO_2 reveals higher activity for doped TiO_2, for UV irradiation. The enhanced adsorption of 4-CP over the catalyst surface and decrease in particle size as a result of Mg^{2+} and Ba^{2+} loadings are suggested to be the cause for higher activity of the catalysts. This study therefore suggests that the introduction of metal nitrate in general and alkaline earth metal nitrate in particular can effectively control the selective crystallization of anatase phase of nano TiO_2. This doped nano TiO_2 exhibits enhanced photocatalytic activity in the degradation of 4-CP.

Zhimang and coworkers (2009) combined both advantages of ordered mesoporous TiO_2 and MgO coating to design an effective photocatalyst for anionic surfactant decomposition. As far as we know, there is rare report about the effect of MgO on the structure and photocatalytic activity of mesoporous TiO_2. To improve the photocatalytic activity of TiO_2 on decomposing anionic surfactants, MgO-coated mesoporous TiO_2 was fabricated by evaporation induced self-assembly (EISA) combined with impregnation method. MgO was uniformly dispersed on the surface of TiO_2, which played the role of stabilizing the ordered mesostructure of TiO_2 and improving the adsorption of anion surfactants, while inhibiting the crystallization of TiO_2. The powders coated with 5 wt.% MgO showed the highest photocatalytic activity for the decomposition of sodium dodecylbenzenesulfonate-6 (DBS).

Yuexiang and coworkers (2007) prepared alkaline-earth metal ion doped TiO_2 photocatalysts by the impregnation and coprecipitation method and a comparative study of the photocatalytic efficiency of pure TiO_2 and doped TiO_2 was perfomed. The effect of doping TiO_2 with alkaline-earth metal ions on its photocatalytic activity was characterized by the photocatalytic generation of hydrogen in suspension. Doping TiO_2 with alkaline-earth metal ions can increase the photocatalytic activity. The optimum doping molar contents of Be^{2+}, Mg^{2+}, Ca^{2+}, Sr^{2+} and Ba^{2+} were 1.25, 1.25, 2.25, 2.25 and 2.25 at. %, respectively. It was found that the activities of the doped photocatalysts depended on the size of the dopant ion and the doping method. When the radius of the doping ion was smaller than or similar to that of Ti^{4+}, the doping effect was obvious; when the radius of the doping ion was much larger than that of Ti^{4+}, the effect of doping was smaller. In particular, when the doping ion was in the

shallow surface, doping was beneficial; while when it was in the deep bulk, the doping was detrimental.

The reaction Figure 3.2, when MgO coated TiO_2 catalyst is exposed to light, TiO_2 particles absorb light to generate electron–hole pairs. Photoexcited electrons in the CB of TiO_2 particle are not energetic enough to inject into the CB of MgO particle, as the CB edge of MgO particle lies far above the CB level of TiO_2. Also the injection of energetic electrons (the hot carrier which has not relaxed to the CB of TiO_2 particle) from TiO_2 to CB of MgO particle can be ruled out considering the band gap energy and energy levels of both MgO (9 eV) and TiO_2 (3.1 eV) (Bandara et al., 2004)

$$MgO/TiO_2 \xrightarrow{hv} MgO/TiO_2(e^-_{CB}, h^+_{VB}) \qquad (3.5)$$

$$MgO/TiO_2(e^-_{CB}, h^+_{VB}) \rightarrow MgO(e^-)/TiO_2(h^+_{VB}) \qquad (3.6)$$

$$MgO(e^-)/TiO_2(h^+_{VB}) \rightarrow [Mg^{2+}--O^{2-}]^-_{LC}/Ti^{IV}OH^{\bullet+}/OH^{\bullet} \qquad (3.7)$$

$$Ti^{IV}OH^{\bullet+}/OH^{\bullet} + Chlorophenol \rightarrow oxidized products \qquad (3.8)$$

$$MgO(e^-)/[Mg^{2+}--O^{2-}]^-_{LC} + O_2 \rightarrow MgO + O^{\bullet-} \qquad (3.9)$$
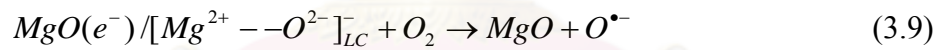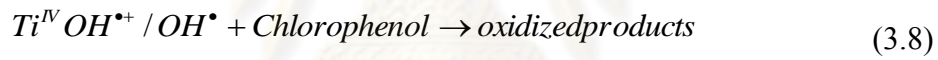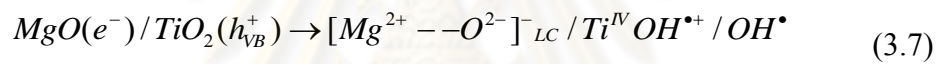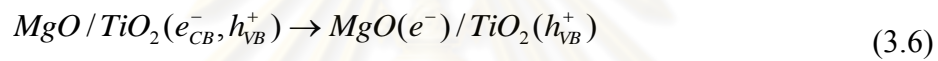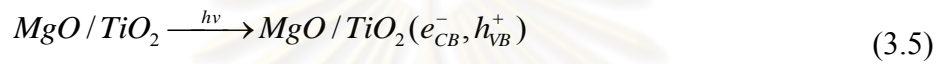
LC represents the lower coordination site.

Figure 3.2 Proposed reaction mechanism of magnesium oxide.

The enhanced photocurrent and photovoltage were explained as a result of thin insulating MgO layer on SnO_2 crystallites acts as a barrier for the recombination of photorelaxed electrons in CB of SnO_2 and oxidized dye molecules. In this study, a thin layer of insulating type oxide, i.e. MgO was coated on TiO_2 as a mean of electron trapping sites and barrier for recombination for photogenerated electrons and holes, which enhanced the overall catalytic activity of the composite TiO_2/MgO system. The photocatalytic activity of TiO_2/MgO for the degradation of 2-chlorophenol, 2,4-dichrolophenol and 4-aminobenzoic acid was presented in the present study and the photosensitized degradation of dyes will be presented in a future article (Bandara et al., 2004)

Chen and coworkers (1999) reported that magnesium ions increased the PC oxidation of 2-chlorophenol in terms of dissolved organic concentration. However, it did not conspicuously increase the mineralization rate of chlorophenols. Magnesium ions enhance the oxidation rate by surface reaction, increasing photo-generated electrons and holes, and inhibiting electron/hole recombination.

Francisco and coworkers (2002) discovered the formation of Ti–O–Mg inhibits the transition of TiO_2 phase and prevents the agglomeration of TiO_2 nano particles and growth of rutile phase. Hence, the entry of Mg^{2+} ions into the TiO_2 lattices suppressed the particle growth and consequently increased the band gap value of nano TiO_2, which minimized the electron–hole recombination during the photocatalytic degradation of organic compounds.

In search of an oxide photocatalyst working under visible light, Hwang and coworkers (2002) discovered that modification of WO_3 by doping with MgO gave interesting photocatalytic properties. In this paper, was reported Mg-doped WO_3 as a novel non-sulfide, visible light-induced photocatalyst, over which H_2 evolves photocatalytically in the presence of a sacrificial agent.

For the control of optical and electronic properties, the divalent and tetravalent metal ion doping to GaN, forming p-type and n-type GaN, have been used, respectively. This offers a possibility of activating GaN, and they have reported in a previous paper that RuO^{2-} dispersed divalent metal ions (Zn^{2+} and Mg^{2+})-doped GaN became stable photocatalysts for overall water splitting, whereas RuO^{2-} dispersed tetravalent metal ions (Si^{4+} and Ge^{4+})-doped GaN showed little photocatalytic activity (Arai et al., 2007).

3.5 Photocatalytic reaction

Hydrogen can be produced from a variety of feedstocks: from fossil resources such as natural gas and coal and from renewable resources such as water and biomass with input from renewable energy resources (e.g. sunlight, wind, wave or hydro-power). Presently, hydrogen is commonly produced from fossil fuels. Natural gas steam reforming is one of the economical hydrogen production processes. Only about 5% of hydrogen is produced from renewable sources, they are called solar hydrogen in this paper. Water electrolysis that can be driven by photovoltaic (PV) cells or wind turbines is an important solar hydrogen production technology today. Other promising solar hydrogen production technologies include solar thermochemical, photoelectrochemical, and photocatalytic hydrogen production. Biomass products, such as plants, microalgaes, and organic wastes, are also renewable sources for solar hydrogen production. The latest developments of individual important renewable hydrogen production technologies are reviewed in the following sections.

3.5.1. Water electrolysis

Water electrolysis is currently the most dominant technology used for hydrogen production from renewable sources because of high energy conversion efficiency.Water, used as a feedstock, is split into hydrogen and oxygen by electricity input as in Equation (3.5.1):

$$H_2O + electricit\, y \rightarrow H_2 + \frac{1}{2}O_2 \qquad\qquad (3.5.1)$$
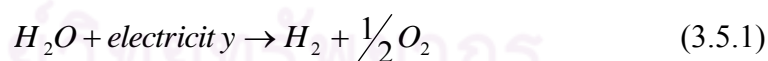
The total energy demand for water electrolysis is increasing slightly with temperature, while the electrical energy demand decreasing. There are three types of water electrolysis available in the industry: 1) alkaline electrolysis, 2) polymer electrolyte membrane (PEM) electrolysis, and 3) high temperature electrolysis. Alkaline electrolysers use an aqueous KOH solution (caustic) as an electrolyte that usually circulates through the electrolytic cells. They are suited for stationary applications and are available at operating pressure up to 25 bar. Alkaline electrolysis is a mature technology allowing remote operation with significant operating experience in industrial applications. The major R&D challenges for the future are the

design and manufacturing of electrolyser equipment at lower costs with higher efficiency and large turndown ratios. PEM electrolysers require no liquid electrolyte, which simplifies the design significantly. The electrolyte is an acidic membrane. PEM electrolysers can be designed for an operating pressure up to several hundred bars, and are suited for both stationary and mobile applications. The main drawback of this technology is the limited lifetime of the membranes. The major advantages of PEM over alkaline electrolysers are higher turndown ratio, increased safety due to the absence of KOH electrolyte, more compact design due to higher current densities and higher operating pressures. The PEM electrolysers currently available are not as mature as alkaline electrolysers with relatively high cost, low capacity, poor efficiency and short lifetime. It is expected that the performance of PEM electrolysers can be improved significantly by materials development and cell stack design. High temperature electrolysis is based on technology from high temperature fuel cells. The electrical energy needed to split water at 1000ºC is reduced considerably compared to hydrogenproduction at 100ºC. Thismeans that high temperature electrolysers can operate at significantly higher overall process efficiencies than regular low temperature electrolysers. A typical technology is solid oxide electrolysers cell (SOEC). This electrolyser is based on the solid oxide fuel cell (SOFC), which normally operates at 700–1000ºC. At these temperatures the electrode reactions aremore reversible, and the fuel cell reaction can more easily be reversed to an electrolysis reaction. For the SOEC, the main R&D needs are related to materials development and thermo-mechanical stress within the functional ceramic materials, which is similar to the main challenges for the SOFC.

3.5.2. Thermochemical water splitting and biomass decomposition

Solar thermochemical cycles are alternative technologies for solar energy utilization. By using trough, dish, or tower concentrators, solar energy can be collected and concentrated to high energy fluxes and high temperature above 2000 K. The thermal energy can be used to activate chemical reactions with feedstocks, such as water, biomass, and fossil fuels, to produce hydrogen. Solar thermochemical cycles suitable for renewable hydrogen production include: 1) water thermolysis, 2) thermochemical water splitting, and 3) thermochemical biomass decomposition.

3.5.2.1. Solar water thermolysis

Solar water thermolysis is the direct dissociation of water into hydrogen and oxygen gas by using concentrated solar thermal energy at a high temperature about 3000 ℃. At this temperature 10% of the water is decomposed and the remaining 90% can be recycled. The process is conceptually simple, but operating at such high temperature requires special material selection. The efficiency is low mainly because of re-radiation loss and energy loss in gas separation by rapid quenching. The gas separation process will also generate explosive mixtures.

3.5.2.2. Solar thermochemical water splitting

To reduce the temperature many thermochemical cycles for high temperature splitting of water have been suggested. The chemical reactions involved in 2-step water splitting thermochemical cycles for hydrogen production are shown below:

$$M_X O_Y \rightarrow xM + \frac{y}{2} O_2 \qquad (3.5.2)$$

$$xM + yH_2O \rightarrow M_X O_Y + yH_2 \qquad (3.5.3)$$

Or

$$M_X O_Y \rightarrow M_X O_Y + O_2 \qquad (3.5.4)$$

$$M_X O_Y + H_2O \rightarrow M_X O_Y + H_2 \qquad (3.5.5)$$
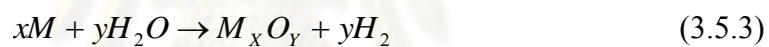
Where M is a metal and MxOy and $M_{x0}O_{y0}$ are the corresponding metal oxides. Since O_2 and H_2 are produced in two different steps, no gas separation is needed. However, separation of metal produced in the first step is needed to avoid re-oxidation. Candidatemetal oxides include TiO_2, ZnO, Fe_3O_4, MnO, MgO, Al_2O_3, and SiO_2. Besides 2-step cycles, 3-step cycles, such as iodine/sulfur (I/S) cycles, and 4-step cycles, such as UT-3 cycles, have also been received extensive research interests in recent years. The maximum theoretical efficiency of solar thermochemical cycles for hydrogen production was estimated to be 49.5%, while currently the achievable efficiency is below 2%.

3.5.2.3. Solar thermochemical biomass decomposition

All energy crops, agricultural residues, organic wastes, forestry waste, industrial wastes, and municipal wastes are categorized as biomass products. Biomass is potentially a reliable energy source for hydrogen production. It is renewable, abundant, and easy to use. As CO_2 emitted during biomass conversion process is trapped and consumed by green plants via photosynthesis, biomass is CO_2 neutral in a complete life cycle.

Pyrolysis and gasification are the two thermochemical processes for biomass energy conversion. Pyrolysis process involves heating of biomass (solid charcoal, liquid oil, or gas compounds) at 650–800 K at 0.1–0.5 MPa in the absence of air. The products of pyrolysis include: 1) gases, including H_2, CH_4, CO, CO_2 and other gases, 2) acetone, acetic acid, and other liquid products, and 3) solid products, such as char, carbon, and other inert materials. Hydrogen gas can be obtained if operation temperature is high and sufficient volatile phase residue time is maintained. The hydrogen production rate can be further improved by steam reforming,

$$CH_4 + H_2O \rightarrow CO + 3H_2 \tag{3.5.6}$$

And water–gas shift reaction,

$$CO + H_2O \rightarrow CO_2 + H_2 \tag{3.5.7}$$
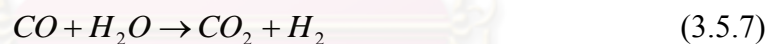
Gasification, on the other hand, is the heating of biomass particles at above 1000 K with partial oxidation for gas production. The gases produced can be steam reformed to produce hydrogen followed by water–gas shift reaction to further enhance hydrogen production.

When biomass has high moisture content above 35%, it is likely to gasify biomass in a supercritical water (SCW) condition. By heating water to a temperature above its critical temperature (647 K) and compressing it to a pressure above its critical pressure (22 MPa), biomass is rapidly decomposed into small molecules or gases in a few minutes at a high efficiency. Supercritical water gasification (SCWG) is therefore a promising process to gasify biomass with high moisture contents with a high gasification ratio (100% achievable) and a high hydrogen volumetric ratio (50% achievable). In recent years, extensive research has been carried out to evaluate the

suitability of various wet biomass gasification in SCW conditions. Although, the works have been mostly on a laboratory scale and are still in the early development stage, the technology has already shown its economic competitiveness with other hydrogen production methods. Spritzer and Hong have estimated the cost of hydrogen production produced by SCWG to be about US$3/GJ (US$0.35/kg).

3.5.2.4. Photoelectrochemical and photocatalytic water splitting

According to Veziroglu, the method of photoelectrochemical and photocatalytic water decomposition using solar energy is probably the most promising method for the hydrogen production. This view has been supported by a recent comprehensive review on hydrogen production. When a semiconductor is irradiated by photons having energy equal to or above the band gap energy, electrons can be promoted from the valence band to the conduction band, leaving a positively charged hole in the valence band. If the conduction band edge is more negative than the hydrogen production level and the valence band edge is more positive than the oxygen production level, the photogenerated electron/hole pairs are able to decompose water into oxygen and hydrogen. Presently, the hydrogen production rate is still low due to the following reasons: 1) quick electron/hole recombination in the bulk or on the surface of semiconductor particles, 2) quick back reaction of oxygen and hydrogen to form water on the surface of catalyst, and 3) inability to utilize visible light.

Addition of electron donors and noble metal loading can enhance hydrogen production significantly due to reduction in charge recombination. Addition of carbonate salts can inhibit back reaction on the catalyst surface. Semiconductors treated by dye sensitization and metal ion-implantation can extend the useful spectrum to the visible range so that the solar energy utilization is increased significantly. Separation of hydrogen gas is required in photocatalytic hydrogen production as oxygen and hydrogen are produced simultaneously.

This can be achieved by employing a photoelectrochemical system, in which hydrogen and oxygen are produced at different electrodes. It is expected that photocatalytic and photoelectrochemical hydrogen production, although still under active R&D, will play an important role in future hydrogen economy.

3.5.2.5. Biological hydrogen production

Biological hydrogen production is presently in the early development stage of laboratory-scale testing. The production processes can be divided into: 1) direct biophotolysis, 2) indirect biophotolysis, 3) biological water–gas shift reaction, 4) photo- fermentation, and 5) dark fermentation. The processes are controlled by hydrogen-producing enzymes, namely, reversible hydrogenase and nitrogenase. In direct biophotolysis, microalgae, such as green algae and Cyanobacteria, absorb light energy and generate electrons. The electrons are then transferred to ferredoxin (FD) using the solar energy absorbed by photosystem I. Then, hydrogenase can accept electrons from FD to produce hydrogen. However, direct biophotolysis is sensitive to oxygen and thus difficult to sustain hydrogen production. The indirect biophotolysis can overcome this problem by producing hydrogen and oxygen at different stages to resolve the issue of oxygen sensitivity.

In biological water–gas shift reaction, some photoheterotrophic bacteria, such as Rhodospirillum rubrum, can survive in the dark by using CO as the sole carbon source to generate adenosine triphosphate (ATP) coupling the oxidation of CO with the reduction of H^+ to H_2. In photo-fermentation, photosynthetic bacteria produce hydrogen through the activity of their nitrogenase using solar energy and organic acid or biomass. The drawbacks of photofermentation are 1) high energy demand for the use of nitrogenase enzyme, 2) low solar energy conversion efficiency, and 3) substantial land need for anaerobic photobioreactors.

Alternatively, in dark fermentation, anaerobic bacteria and some microalgae, such as green algae on carbohydrate-rich substrates, can produce hydrogen in a dark environment. Since solar irradiation is not a requirement, dark fermentation is more versatile. In the project of Basic Research of Mass Hydrogen Production using Solar Energy, the emphasis has been paid on fundamental theories of hydrogen production from solar energy especially visible light using thermochemical decomposition of biomass and water, or/and using photolysis of water. The main research contents of this project include the principles for the construction of novel hydrogen production system and the related fundamental science problems, the design, preparation, characterization and action mechanism of catalysts, and the theory for mass

production of two specific hydrogen production methods and systems. Some progresses have been achieved and will be reported in the next section.

CHAPTER IV

EXPERIMENTAL

4.1 Chemicals

The details of chemicals used in this research are listed below.

- Titanium (IV) isopropoxide ($C_{12}H_{28}O_4Ti$) 97% available from Sigma-Aldrich.

- Ethanol (C_2H_5OH) 99.99% available from Merck.

- Methanol (CH_4OH) 99.9% available from Burdick and Jackson

- Nitric acid (HNO_3) 70% available from Asia Pacific Specialty Chemicals Limited.

- Boric acid (H_3BO_3) available from Sigma-Aldrich.

- Magnesium chloride ($MgCl_2.6H_2O$) available from Ajax Finechem Pty Ltd.

4.2 Catalyst preparation

4.2.1 Preparation of boron and magnesium doping on TiO_2 support

Titanium dioxide was prepared by the acid-catalyzed sol-gel method. First, the sol was prepared by mixing titanium isopropoxide with DI water and 70% nitric acid at room temperature while being stirred, until clear solution or around 72 hours. For 166.8 ml of titanium isopropoxide, 2000 ml of water, and 14.44 ml of nitric acid were used. For doping boron was mixed varied ratio 0 to 2% (w/w) and magnesium was fixed ratio 1% (w/w) with TiO_2. A certain amount of boric acid (H_3BO_3) and magnesium chloride ($MgCl_2.6H_2O$) were dissolved in 50 ml of titania sol, keeping the reaction mixture vigorously magnetically stirred to form sol and was stirred continuously for 2 h. To remove solvents, the catalyst solution was dried at 110ºC for 24 hours. Finally, titanium dioxide catalyst was fired at 350ºC for two hours.

4.3 Photocatalytic reactor

Figure 4.1 shows a schematic diagram of a photocatalytic reactor used in this study. The vertical tubular batch reactor was made of Pyrex and has a volume of 150 ml. The reactor was 4 cm in diameter and 24 cm long. Two tubes were placed inside the reactor was connected with glass valve to argon cylinder and was used to feed argon carrier gas. The other valve was used vent argon carrier gas.

In the part of UV light, titanium dioxide photocatalyst was suspended by means of a magnetic stirrer and irradiated with eight UV light bulbs (Philips actinic blue), each having a power of 20 W. In the part of visible light, irradiated with eight day light bulbs (Philips), each having a power of 18 W, which the intensity of UV light bulbs and day light bulbs were measured by two light sensors.
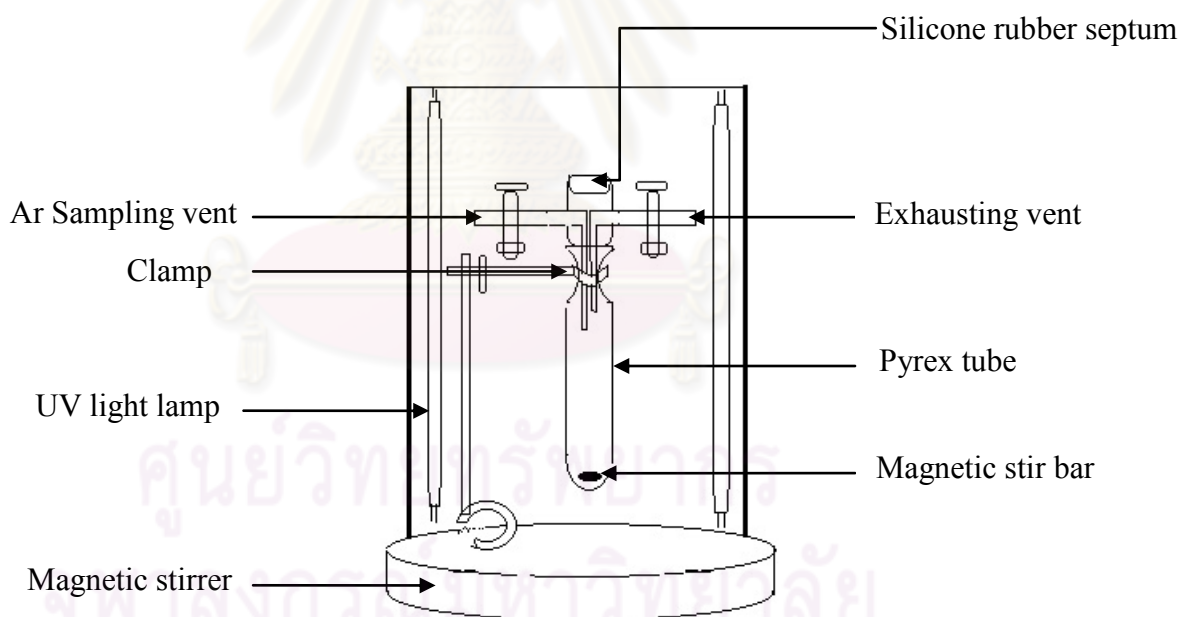
Figure 4.1 Experiment set-up of photochemical reactor.

Table 4.1 Operating condition for the gas chromatograph

Gas Chromagraph	SHIMADZU GC-8A
Detector	TCD
Column	Molecular sieve 5A
- Column material	SUS
- Length (m)	2
- Outer diameter (mm)	4
- Inner diameter (mm)	3
- Mesh range	60/80
- Maximum temperature (ºC)	350
Carrier gas	Ar (99.999%)
Carrier gas flow (ml/min)	30
Initial column temperature (ºC)	60
Final column temperature (ºC)	60
Injector temperature (ºC)	100
Detector temperature (ºC)	100
Current (mA)	70
Analyzed gas	Hydrogen

4.4 Photocatalytic reaction

The photocatalytic activity was performed over 0.3 g of titanium dioxide catalyst was suspended in 50 ml of water/methanol solution in the vertical tubular batch reactor and put magnetic stir bar in pyrex tube reactor. The volume ratio of water to methanol was 4:1. Ultra high purity argon was used to purge the reactor for 120 minutes to remove oxygen inside the reactor after that closed the argon gas and opened magnetic stirrer and eight UV light bulbs. The splitting water reaction was carried out for 5 h and the reaction gas mixture was periodically sampled every half hour to analyze amount to hydrogen released was determined by a Shimazu GC-8A gas chromatograph equipped with a thermal conductivity detector. The operating conditions for the gas chromatograph are displayed in Table 4.1.

4.5 Catalyst Characterization

The catalysts were characterized by various techniques.

4.5.1 X-ray diffraction analysis (XRD)

The XRD spectra were measured by using a SIEMENS D5000 X-ray diffractometer using Cu K_α radiation with a Ni filter. The crystallite size of titanium dioxide was determined from the width at half-height of the (101) diffraction peak of anatase using the Scherrer equation. The condition of the measurement was performed over the 2θ range of 20º to 80º and the resolution was 0.04º. A total of 10 scans were performed for each sample.

4.5.2 Surface area measurement

The specific surface area of titanium dioxide was measured according to the single point BET method, by using nitrogen as the adsorbate. The weight of the sample was 0.2 g. And the sample was degassed at 200ºC prior to the measurement.

4.5.3 UV-visible absorption spectroscopy (UV-Vis)

To study the light absorption behavior of the catalysts, the absorbance spectra of the catalysts in the wavelength range of 200-800 nm were obtained using a Perkin Elmer Lambda 650 spectrophotometer. The step size for the scan was 1 nm. $BaSO_4$ was used as a blank for the measurement. The band gap (E_g) of the sample was determined by the following equation (4.1):

$$E_g = \frac{1240}{\lambda} \qquad (4.1)$$

Where E_g is the band gap (eV) of the sample, λ (nm) is the wavelength of the onset of the spectrum.

4.5.4 Photoluminescence spectroscopy (PL)

Photoluminescence spectra were obtained using a JASCO FP-6200 Spectrofluorometer at room temperature. The amount of sample was used 0.5 g. The sample was mixed with 10 ml of ethanol and was sonicated for two hours. The excitation wavelength was 370 nm with an excitation bandwidth of 5 nm and an emission bandwidth of 10 nm. The measurement was performed over the range of wavelength between 200 and 800 nm with a step size of 1 nm.

4.5.5 X-ray photoelectron spectroscopy (XPS)

The XPS analysis was performed using an AMICUS photoelectron spectrometer equipped with a Mg K_α X-ray as a primary excitation and a KRATOS VISION2 software. XRS elemental spectra were acquired with 0.1 eV energy step at a pass energy of 75 kV. The C_{1s} line was taken as an internal standard at 285.0 eV. Photoemission peak areas were determined after smoothing and background subtraction using a linear routine. Deconvolution of complex spectra were done by fitting with Gaussian (70%)-Lorentzian (30%) shapes using a VISION 2 software that came with the XPS system.

4.5.6 Inductively-coupled plasma atomic emission spectroscopy (ICP-AES)

Boron and magnesium contents were measured using a Perkin Elmer Optical Emission Spectrometer Optima 2100 DV. To digest the sample, the catalyst was dissolved in 10 ml of 50% HF solution. The mixture was heated to 50ºC and stirred for two hours. After the catalyst was completely digested, the solution was diluted to a volume of 100 ml.

4.5.7 Electron spin resonance spectroscopy (ESR)

ESR measurements were carried out using a JEOL JES-RE2X electron spin resonance spectrometer to determine the amount of Ti^{3+} surface defect in TiO_2. Recorded spectra were scanned and were converted to a g-valve scale referring to Mn^{2+} marker.

4.5.8 Fourier transform infrared spectroscopy (FT-IR)

FT-IR analysis of modified TiO_2 was carried out in a Nicolet model 6700 of the IR spectrometer using the wavenumber ranging from 400-4000 cm^{-1} with a resolution of 4 cm^{-1}.

4.5.9 Scanning electron microscope with energy-dispersive x-ray analyzing system (SEM-EDX)

Scanning electron microscopy (SEM) and Energy dispersive X-ray spectroscopy (EDX) was used to determine the morphology and elemental distribution of the catalyst particles. Model of SEM: JEOL mode JSM-5800LV and EDX was performed using Link Isis Series 300 program at the Scienctific and Technological Research Equipment Center, Chulalongkorn University (STREC).

CHAPTER V

RESULTS AND DISCUSSION

The results in this chapter are divided into three sections. Section 5.1 describes the properties and photocatalytic activities of titanium dioxide doped with boron. Section 5.2 describes the properties and photocatalytic activities of Titanium dioxide doped with boron and magnesium.

5.1 Properties and photocatalytic activity of titanium dioxide doped with boron.

5.1.1 Crystallite phase and size

The phase identification of titanium dioxide was based on the results from X-ray diffraction analysis (XRD). The XRD patterns of various titanium dioxides doped with boron samples were displayed in Figure 5.1. The diffraction peak at 2θ values of 26º, 37º, 48º, 55º, 56º, 62º, 69º, 71º, and 75º indicated that titanium dioxide was primarily in the anatase phase (Eakachai, 2007). Small amounts of brookite and rutile were detected in some samples. By contrast with pure titanium dioxide, the partial substitution of O atoms for B atoms causes a decrease of the titanium dioxide content in B-doped titanium dioxide samples and the amount of anatase particles also decreases to some extent (Na et al., 2008). The average sizes of the crystallites calculated from the broadening of corresponding X-ray diffraction peaks using the Scherrer formula were about 4.7 nm for pure titanium dioxide and all boron doped samples were approximately range of 4.8-5.1 nm that boron doing indicated the growth of anatase crystallite (from Table 5.1).

A-Anatase R-Rutile B-Brookite
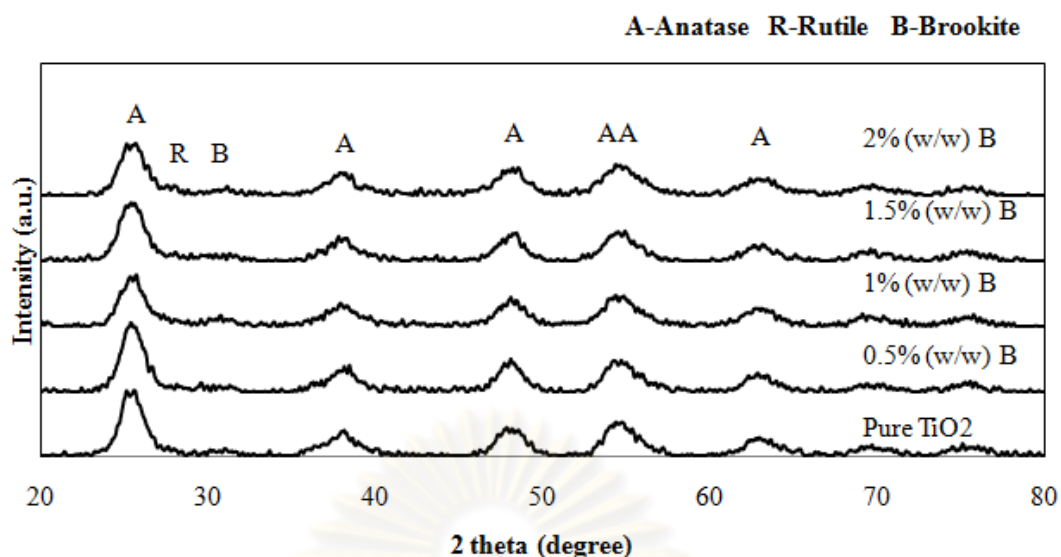
Figure 5.1 XRD patterns of titanium dioxide doped with various amount of boron

5.1.2 Specific surface area

Specific surface areas of the catalyst were determined from nitrogen adsorption isotherms and were displayed in Table 5.1. Pure titanium dioxide possessed the largest specific surface area. Upon addition of boron, specific surface area decreased. However, the amount of boron doping appeared to have no significant effects on specific surface area of the catalyst.

Table 5.1 Crystallite size and specific surface area of titanium dioxide with various amounts of B doping

B doping (% (w/w))	Crystallize size (nm)	Surface area (m^2/g)
Pure Titanium dioxide	4.7	194.8
0.5	5.1	186.5
1	4.9	185.1
1.5	5.0	180.0
2	4.8	185.0

5.1.3 Metal content

Percentage of boron on titanium dioxide catalysts was determined by Inductively couple plasma atomic emission spectroscopy (ICP-AES). The boron contents in various catalyst samples were listed in Table 5.2. As seen in Table 5.2, the boron content determined that was ICP-AES was lower than the expected boron content that was calculated for use during the sol-gel preparation step. This discrepancy could be a result of incomplete digestion of ICP-AES sample and uneven distribution of metal on titanium dioxide.

5.1.4 Light absorption characteristics

UV-visible light absorption characteristics of various titanium dioxide doped with boron were presented in Figure 5.2. It was seen that the major absorbance at wavelengths less than 400 nm was pertaining to the intrinsic band gap absorption of titanium dioxide (3.2 eV). The boron doped samples all exhibit red shifts in the band gap transition and the absorption edge in the spectrum of sample with 2% of boron has the highest absorption. In addition, the boron doped samples also exhibit stronger absorption in the UV–vis range. The results of the absorption feature suggest that boron doped titanium dioxide could be activated by visible light and might exhibit enhanced photoresponse under UV light as well.

The addition of boron gave rise to a new absorption appears at around 400 to 600 nm. The boron-titanium dioxide photocatalyst had narrow band gap, showed optical absorption and photocatalytic activity in the visible region. Boron was incorporated into the crystal structure of TiO_2, which could narrow the band gap of titanium dioxide (Qincai et al., 2008). As seen in Figure 5.2, these UV-vis results of addition boron showed a slight red-shift and displayed stronger absorption in both UV and visible range in comparison with pure titanium dioxide.

For the comparation band gap as shown in Table 5.3, which the boron doping has the reduced band gap energy. Thus, the boron doping effect to the activated visible region.

Table 5.2 Boron content as measured from ICP-AES, on titanium dioxide doped with various amount of boron

Calculated B doping (% (w/w))	Measured B content (% (w/w))
0	0
0.5	0.464
1	0.879
1.5	1.214
2	1.871
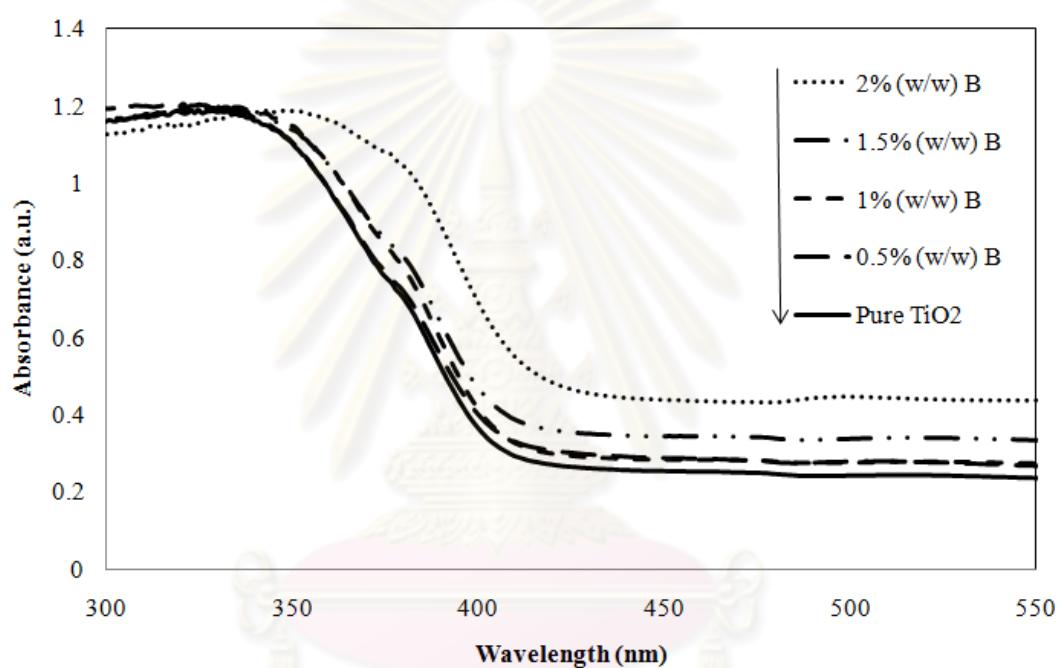
Figure 5.2 UV-visible absorption characteristics of titanium dioxide doped with various amount of boron.

Table 5.3 The comparison band gap from UV-vis spectra of titanium dioxide doped with various amount of boron.

Catalyst	wavelength (nm)	band gap (eV)
Pure TiO$_2$	421	2.95
0.5	422.43	2.94
1	423.32	2.93
1.5	425.57	2.91
2	437.92	2.83

5.1.5 Photoluminescence measurement

Photoluminescence emission spectrum was used to investigate the efficiency of charge carrier trapping, immigration, and transfer, and to understand the late of electrons and hole in titanium dioxide since photoluminescence emission resulted from the recombination of free carriers. Figures 5.3 displayed the photoluminescence spectra for the catalysts that were excited by irradiation with a wavelength of 350 nm at room temperature. Two main emission peaks were observed at wavelengths of 410 and 467 nm, which corresponded to band gap energies of 3.0 and 2.7 eV, respectively. The first emission peak was ascribed to the emission of band gap transition (or the recombination of photogenerated electrons and holes) at a wavelength of 410 nm. The second emission peak was ascribed to the emission signal originated from the energy levels of defects in the band gap, such as oxygen vacancies formed during sample preparation at a wavelength of 467 nm. The oxygen vacancies were generated because of partially incomplete crystallization. The variation in photoluminescence emission spectrum intensity resulted from the change of defect state on the shallow level of the titanium dioxide surface (Zhao et al., 2007). Figure 5.3 revealed that the photoluminescence signal of pure titanium dioxide was the highest among all the samples. Upon addition of boron (from 0.5% (w/w) to 2% (w/w)), photoluminescence signals were decreased. It could be observed that the photoluminescence intensity of 2% (w/w) sample was significantly lower than the lower boron content. This result indicated that the recombination of charge carriers was effectively suppressed after boron doped on titanium dioxide.
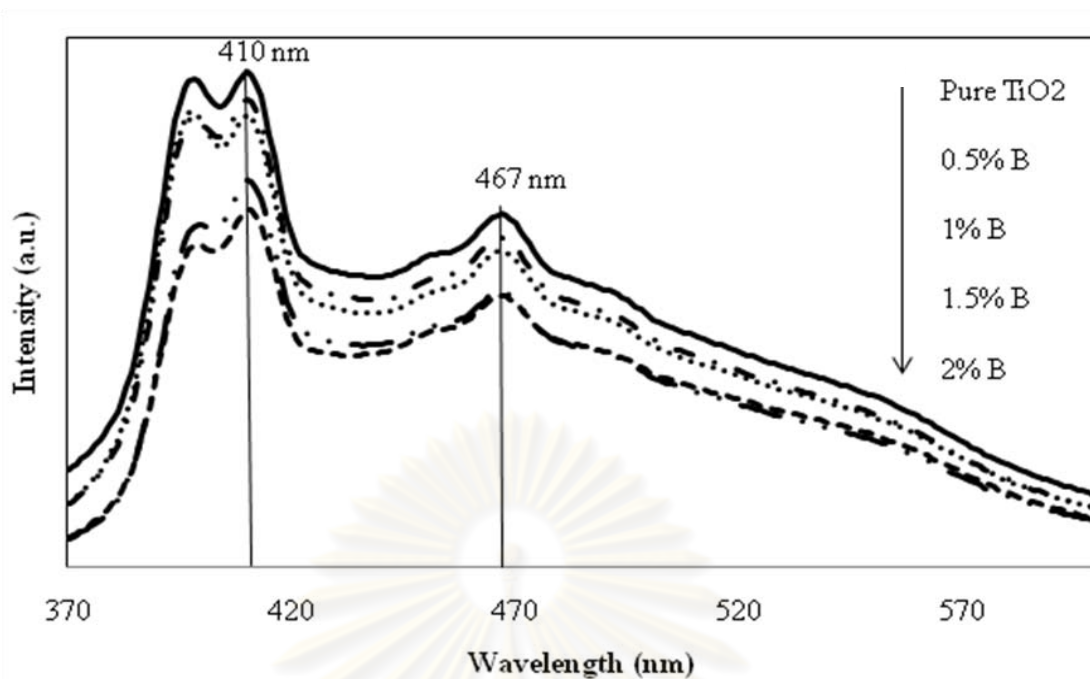
Figure 5.3 Photoluminescence emission signals in a range of 370-600 nm for titanium dioxide doped with various amount of boron.

5.1.6 Lighting Instrument.

Intensity of both light bulbs was measured by Light sensor of both UV and visible range, as shown in Table 5.4.

Table 5.4 The light bulb properties of using the photocatalytic activity

Type of light bulb	Type of light	Number of bulb	Power (W)	Intensity by sensor UV light (SED 005) (%)	Intensity by sensor visible light (SED 033) (%)
Actinic blue* (Philips)	UV light (250-400 nm)	8	20	99.97	0.03
Day light** (Philips)	Visible light (400-700 nm)	8	18	0.01	99.99

5.1.7 X-ray photoelectron spectroscopy (XPS)

The XPS spectra for B/TiO_2 samples were recorded with photon energy of 1256 eV (Mg K_α). For all measurements, the kinetic energies of the emitted electrons in the range of 0-1000 eV were detected. Figure 5.4 a) and b) was showed the XPS spectra of 2% (w/w) B. Figure 5.4a) revealed that the binding energy (BE) for B1s was 191.9 eV. Base on the previous researches reported in the literature, the binding energies for B1s were 193.6 eV in B_2O_3(B-O bond), 193.0 eV in H_3BO_3(B-O bond), and 187.5 eV in TiB_2(Ti-B bond). This indicated that the boron atoms were not bonded by means of B-Ti-B bond or B-O bond. From figure 5.4b), it could be observed that 2% (w/w) B for Ti2p was 458.9 eV and 464.3, which were attributed to $Ti2p_{3/2}$ and Ti $2p_{1/2}$, respectively. According to the report (Qincai et al., 2008), the BE for $Ti2p_{3/2}$ in TiB_2 was 454.4 eV, thus further confirming that there was no existence of the compound TiB_2. Hence, it was obvious that boron atoms (binding energy = 191.9eV) were doped into lattice, there probably were such structure as Ti-O-B.

5.1.8 Fourier transform infrared spectroscopy (FT-IR)

The FT-IR spectra of $B-TiO_2$ samples fired at 350ºC are shown in Figure 5.5, several peaks at 500-4000 cm^{-1} were observed the peaks of C–O bond at 1026 cm^{-1}, C–O–C bond at 1224 cm^{-1}, C–OH bond at 1370 cm^{-1}, C=O bond at 1740 cm^{-1}, C=C bond at around 1636 cm^{-1}, and a broad peak at the range of 3000–3500 cm^{-1} which is attributed to the O–H stretching vibrations of the C–OH groups and water. The peak at 2336 cm^{-1} can be assigned to the absorption peak of carbon dioxide (CO_2), which is attributed to the (C-C) stretching. Meanwhile, for all doped TiO_2 samples and Pure TiO_2, the broad absorption at low wave numbers (below 1000 cm^{-1}) is attributed to the vibration of Ti–O–Ti bonds in TiO_2 (Yupeng et al., 2011).

Table 5.5 was shown the peak height of C-C bond of only boron doped was calculated from FT-IR spectra, which varied from 1.1 to 19. The best peak height C-C bond as 1% (w/w) B was 19. Visible light activity could be enhanced by presence of carbonaceous species (C–C) occurred in highly condensed and coke-like structure, which could play the role of photosensitizer to induce the visible light absorption and response. Some carbon compounds existed at the photocatalyst, which might be from the precursor of titanium or adsorbed CO_2 in the air (Adriana et al., 2009).
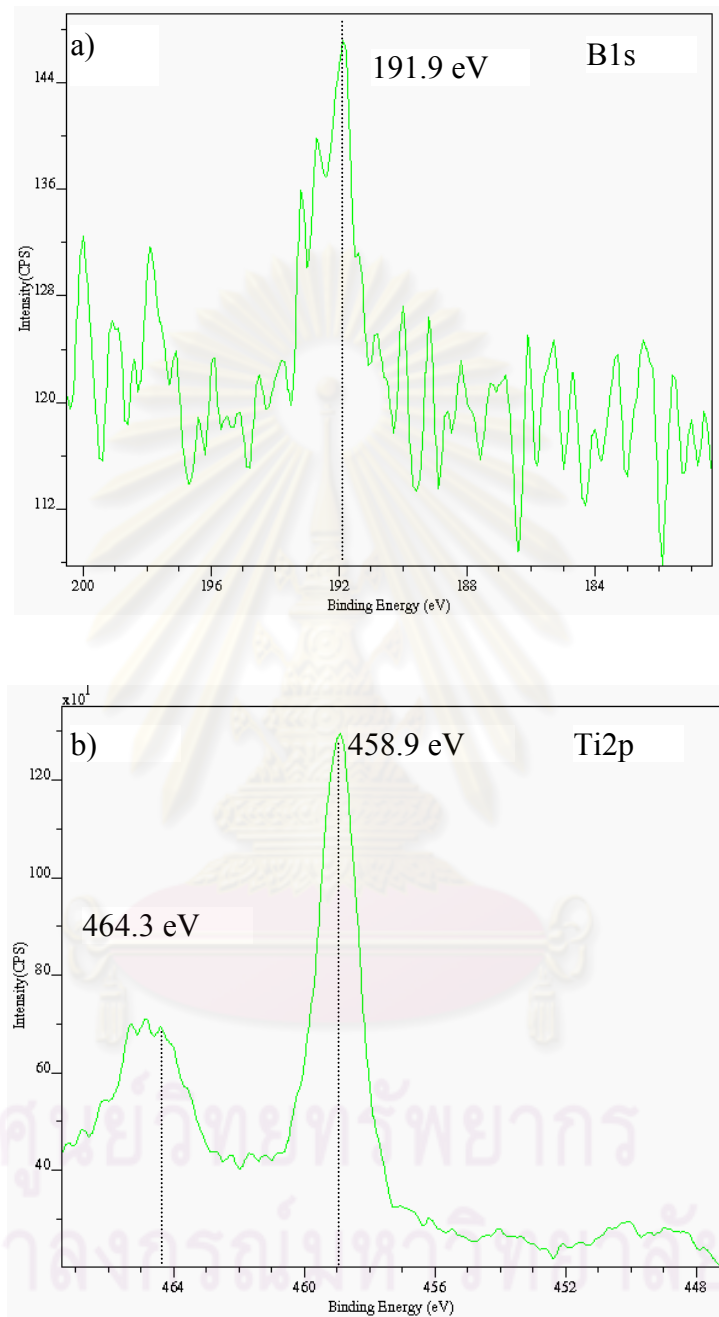
Figure 5.4 XPS spectrum of TiO$_2$ that was doped with 2% (w/w) B : a) B1s, b) Ti2p
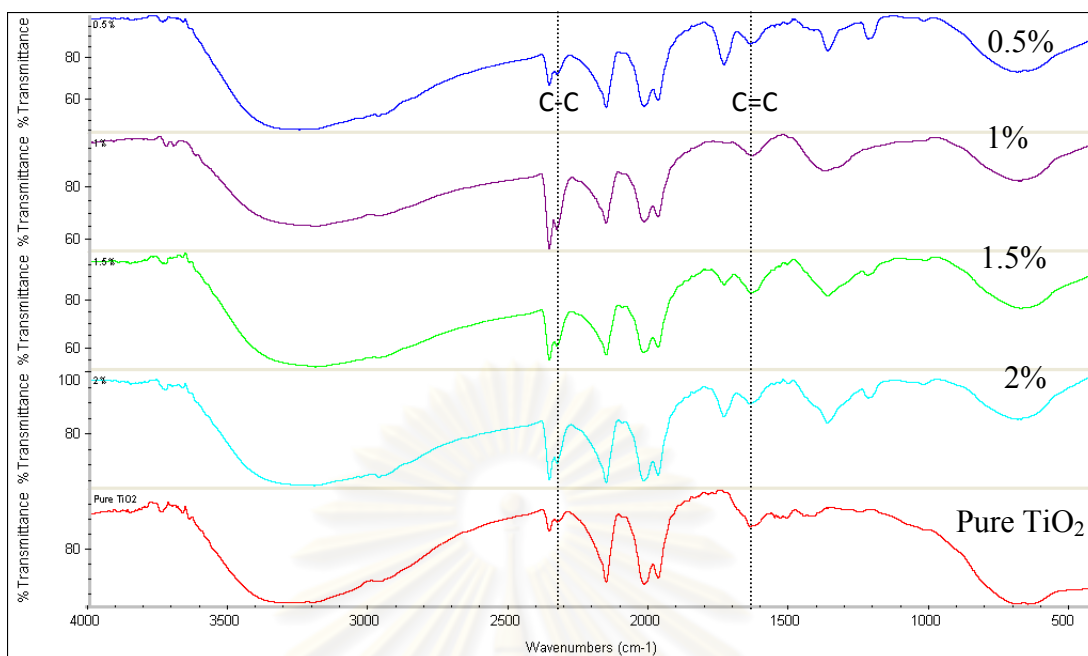
Figure 5.5 FTIR spectra for the only boron doped sample

     5.1.9 Scanning electron microscope with energy-dispersive x-ray analyzing system (SEM-EDX)

     As shown in Figure 5.6 a) and b), was analyzed the amount element of sample TiO_2 and boron doped TiO_2, respectively, as C, O, Mg, and Ti but not show peak the blinding energy (B_E) of B because the B_E value of B was lower than C that could not show the B peak by SEM-EDX. Table 5.6 was shown the different percent of each element in pure TiO_2 and boron doped TiO_2 sample, which was indicated that the amount of carbon in 1% (w/w) B was higher than 2% (w/w) B and pure TiO_2, agreement with FTIR spectra that was shown the carbonaceous species act as a photosensitiser.

Table 5.5 Calculation peak height(C-C) from FTIR spectra for the only boron doped
sample

B doping (% (w/w))	height (C-C)
Pure TiO_2	1.1310
0.5	8.8880
1	18.9960
1.5	14.1110
2	12.3310
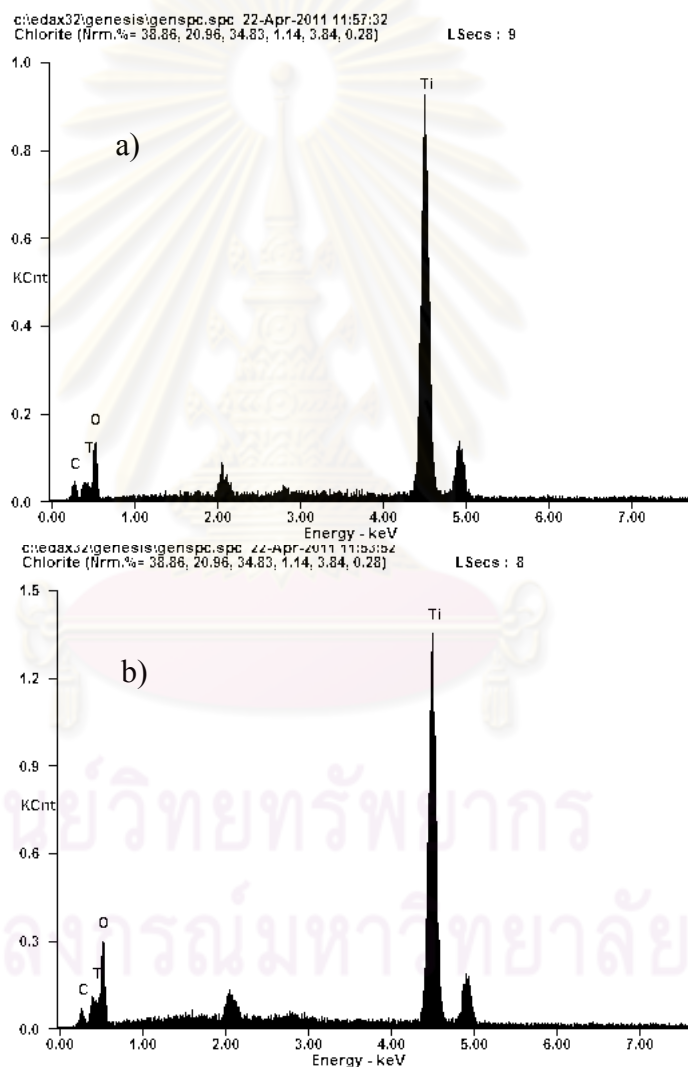
Figure 5.6 SEM-EDX analysis for determine the percent of element the only boron
doped sample : a) Pure TiO_2, b) 1% (w/w) B

Table 5.6 Calculation percent of element by SEM-EDX for the only boron doped sample

Element	C		O		Mg		Ti	
%(w/w)	wt%	at%	wt%	at%	wt%	at%	wt%	at%
Pure TiO$_2$	2.09	5.23	26.78	50.22	-	-	71.13	44.55
1% B	2.77	7.76	17.19	36.10	-	-	80.04	56.14
2% B	2.70	8.29	10.85	24.99	0.22	0.33	86.03	66.17

5.1.10 Photocatalytic activity

- The reaction under UV light irradiation (200-400 nm)

Figure 5.7 showed the amount of hydrogen production from splitting water versus irradiation time under UV light illumination, which was used to test the photocatalytic activity. One could observe that all boron-prepared samples exhibited more photocatalytic activity than pure titanium dioxide under UV light. It could be also seen that the addition of boron sample had an effect on the decomposition of water. This result agreed with the result from photoluminescence measurement. The orders of decreasing activity were 2% (w/w), 1.5% (w/w), 1% (w/w), 0.5% (w/w) B and pure TiO$_2$ and were the same as the order of increasing photoluminescence signals (see Figure 5.3). The photocatalytic reaction depended on the efficient separation of photogenerated charge carriers in titanium dioxide. Therefore, slower recombination of electrons and holes led to higher photocatalytic activity. As a result, the catalyst with the highest activity should produce the smallest signal in photoluminescence measurement. This agreement was also observed in our case.

Among the samples, the best performance was attributed to 2% (w/w) B corresponding to the maximum red shift in the UV–vis diffusive reflectance absorption spectra. It could be calculated that the photocatalytic performance of 2% (w/w) B was almost 6 times higher than that of pure titanium dioxide for decomposition of water under UV light. Obviously, the photocatalytic activity of B doped TiO$_2$ under UV light demonstrated that B doping effect was outstanding. These agreed with the outcome from the UV-vis spectra.

Our results were also in good agreement with the results of Zaleska and coworkers (2009), which studied the photocatalytic activity of obtained powders was estimated by measuring the decomposition of phenol in aqueous solution. The highest photoactivity was observed for the titanium dioxide sample obtained with 2 wt.% boron. The role of boron, unanimous agreement is that transition metals narrow the band gap and at the same time reduce the recombination rate of photogenerated electrons and holes.

- The reaction under visible light irradiation (400-700 nm)

Figure 5.8 showed the amount of hydrogen production from splitting water versus irradiation time under visible light illumination, which was used to test the photocatalytic activity. One could observe that all boron-prepared samples exhibited more photocatalytic activity than pure titanium dioxide under visible light. It could be also seen that the addition of boron sample had an effect on the decomposition of water.

This decreasing signal result from photoluminescence measurement was pure TiO_2, 0.5% (w/w), 1% (w/w), 1.5% (w/w) and 2% (w/w) B, respectively (see Figure 5.3), as same as the order of increasing absorption spectra (see Figure 5.2). Normally in UV light reaction, the mainly characterization method usually analysed by UV–vis diffusive reflectance absorption spectra and photoluminescence measurement. From the among characterization result of the B doped samples, the best performance should be attributed to 2% (w/w) B corresponding to the maximum red shift in the UV–vis diffusive reflectance absorption spectra and lowest photoluminescence signal. On the other hand in visible light, the highest photocatalytic activity performance was 1% (w/w) B and lowest activity was 2% (w/w) B in all B doped samples.

From the mechanistic results discussed so far, one can conclude, that oxygen plays a major role in the photodegradation of pollutant, and two major reaction pathways can be considered (Christian et al., 2001).

1. The carbonaceous species acts as a photosensitiser without participation of the titanium dioxide (Eq.5.1). After excitation of the photosensitiser S, singlet oxygen is formed by a triplet–triplet energy transfer. Alternatively, an electron can be transferred directly fromthe excited photosensitiser to triplet oxygen to generate the

superoxide radical anion $O_2^{\bullet-}$. Both species, singlet oxygen and $O_2^{\bullet-}$, are capable of degrading pollutant.

$$S \xrightarrow{h\nu} {}^1S^* \rightarrow {}^3S^* \xrightarrow{O_2} {}^1O_2$$
$$\downarrow O_2 \qquad\qquad (5.1)$$
$$S^+ + O_2^{\bullet-}$$
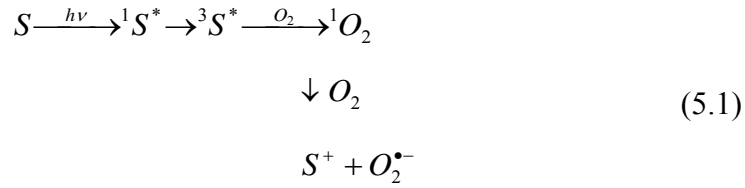
2. The excited photosensitiser injects an electron into the conduction band of titanium dioxide (as shown in Eq.5.2). Subsequently, the electron is transferred to oxygen adsorbed on the semi-conductor surface producing $O_2^{\bullet-}$.

$$S \xrightarrow{h\nu} {}^1S^* \xrightarrow{TiO_2} TiO_2^{\bullet-} + S^+ \xrightarrow{O_2} S^+ + TiO_2 + O_2^{\bullet-} \qquad (5.2)$$
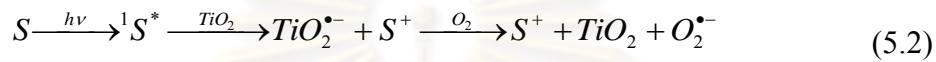
Adriana and coworkers (2009) proposed that Visible light activity could be enhanced by presence of carbonaceous species (C–C) occurred in highly condensed and coke-like structure, which could play the role of sensitizer to induce the visible light absorption and response. From analysis enabled detection of carbonaceous species on the TiO_2 surface. C=O, C–OH, and C–C_{arom} peaks appeared, where the surface C–C_{arom} structures were best represented (12.2 at.% for the BE_G(2), 2% (w/w) B sample). Carbon content in the surface layer varies from 9.8 to 18.5 at.% and was independent of boric acid triethyl ester used for modification.

From previous research, Adriana and coworkers (2008) suggested that however, photoactivity of our samples under visible light could originate from both carbon and boron presence, regarding the role of carbon. The sample BE-H(10), 10% (w/w) B, which revealed highest visible-light absorption, was not active under visible light. Visible-light absorption of sample BE-H(10) could result from defects and/or impurities (e.g. carbon which presence was evidenced by dark-brownish color).

However, photoactivity under visible light of all samples could originate from both carbon and boron presence, see from FT-IR result (Figure 5.5), regarding the role of carbon as a photosensitiser of C-C bond. These peak height of FT-IR results in Table 5.5, could be listed as follows: 1% (w/w) B > 1.5% (w/w) B > 2% (w/w) B > 0.5% (w/w) B, agreed with photocatalytic activity.

As shown in Figure 5.8, the visible light induced H_2 production was remarkably enhanced by doping TiO_2 with B. Sample of 1% (w/w) B exhibits the

highest activity with a hydrogen production rate as about 7 times of pure titanium dioxide for decomposition of water under visible light.
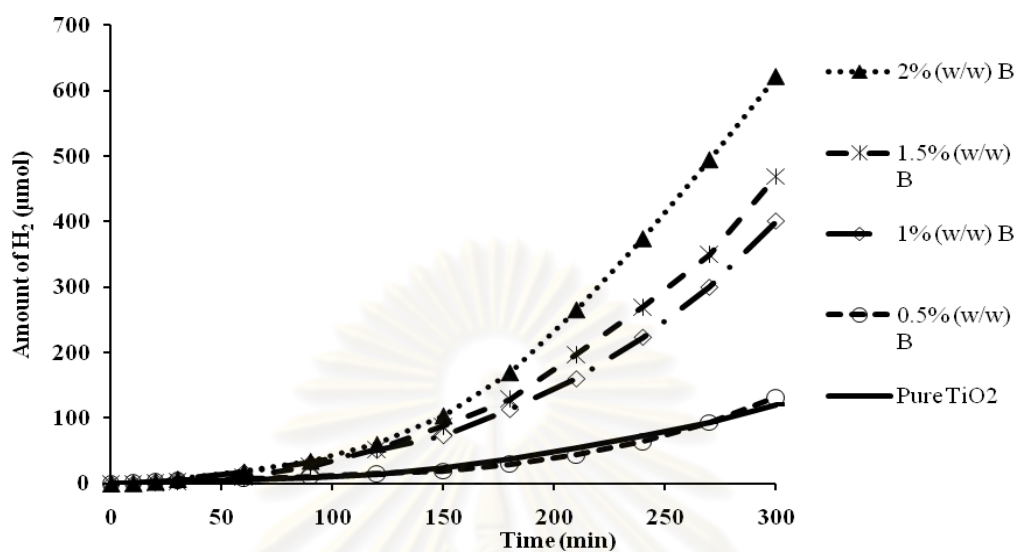

Figure 5.7 Amount of hydrogen produced from photocatalytic water splitting over titanium dioxide doped with various amount of boron under UV light irradiation.
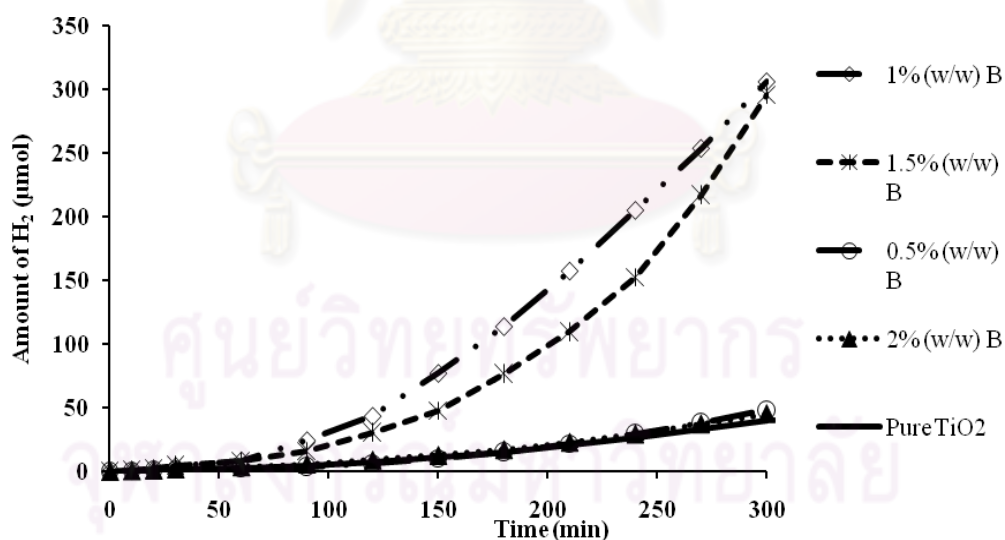

Figure 5.8 Amount of hydrogen produced from photocatalytic water splitting over titanium dioxide doped with various amount of boron under day light irradiation**.**

5.2 Properties and photocatalytic activity of titanium dioxide doped with boron and 1% (w/w) magnesium.

5.2.1 Crystallite phase and size

The phase identification of titanium dioxide was based on the results from X-ray diffraction analysis (XRD). The XRD patterns of various titanium dioxides doped with boron and 1% (w/w) magnesium samples were displayed in Figure 5.9. The diffraction peak at 2θ values of 26º, 37º, 48º, 55º, 56º, 62º, 69º, 71º, and 75º indicated that titanium dioxide was primarily in the anatase phase (Eakachai, 2007). Small amounts of brookite and rutile were detected in some samples. By contrast with pure titanium dioxide, the partial substitution of O atoms for B atoms causes a decrease of the titanium dioxide content in B-doped titanium dioxide samples and the amount of anatase particles also decreases to some extent (Na et al., 2008). No significant changes in the diffraction peak positions were observed. The average sizes of the crystallites calculated from the broadening of corresponding X-ray diffraction peaks using the Scherrer formula were about 4.7 nm for pure titanium dioxide and all boron doped samples were approximately range of 4.7-5.4 nm that boron doing indicated the growth of anatase crystallite (from Table 5.7).

5.2.2 Specific surface area

Specific surface areas of the catalyst were determined from nitrogen adsorption isotherms and were displayed in Table 5.7. Pure titanium dioxide possessed the largest specific surface area. Upon addition of boron and magnesium, specific surface area decreased. However, the amount of boron doping appeared to have no significant effects on specific surface area of the catalyst.
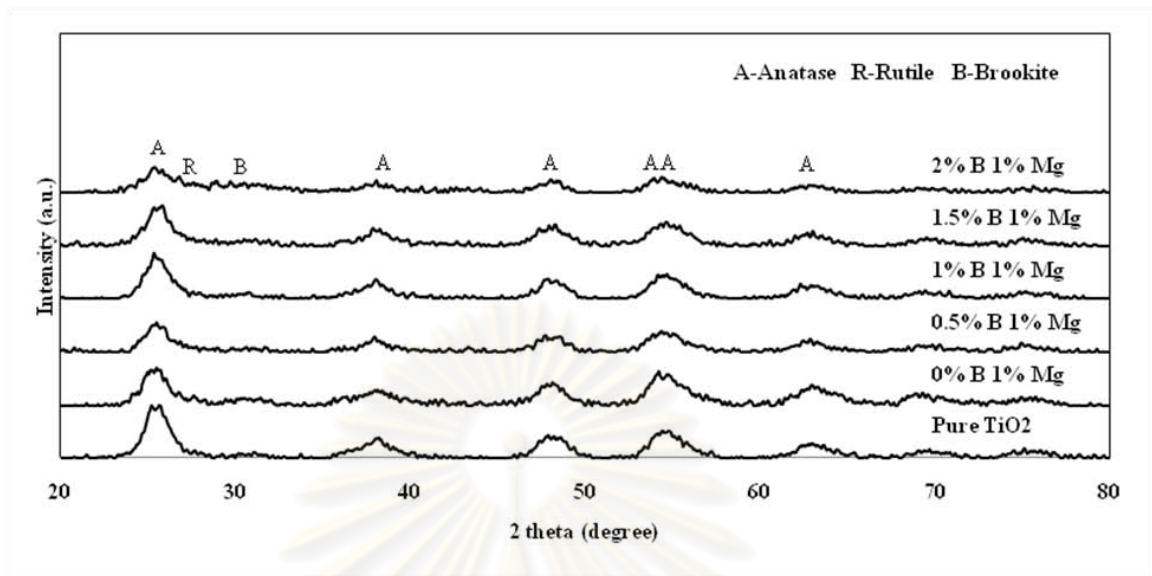
Figure 5.9 XRD patterns of titanium dioxide doped with various amount of boron and 1% (w/w) Mg.

Table 5.7 Crystallite size and specific surface area of titanium dioxide with various amounts of B and 1% (w/w) Mg doping.

B doping (% (w/w))	Crystallize size (nm)	Surface area (m²/g)
Pure Titanium dioxide	4.7	194.8
0 (1% Mg)	4.9	150.8
0.5	5.0	184.1
1	5.0	153.0
1.5	5.4	142.6
2	4.7	164.7

Table 5.8 Boron and 1% (w/w) magnesium content as measured from ICP-AES, on titanium dioxide doped with various amount of boron.

Calculated B doping (% (w/w))	Measured B content (% (w/w))	Measured Mg content (% (w/w))
0 (1% Mg)	0	0.896
0.5	0.416	0.863
1	0.747	0.832
1.5	1.183	0.885
2	1.671	0.901

5.2.3 Metal content

Percentage of boron on titanium dioxide catalysts was determined by Inductively couple plasma atomic emission spectroscopy (ICP-AES). The boron and 1% (w/w) magnesium content in various catalyst samples were listed in Table 5.8. As seen in Table 5.8, the boron and magnesium content determined that was ICP-AES was lower than the expected boron and magnesium content that was calculated for use during the sol-gel preparation step. This discrepancy could be a result of incomplete digestion of ICP-AES sample and uneven distribution of metal on titanium dioxide.

5.2.4 Light absorption characteristics

UV-visible light absorption characteristics of various titanium dioxide doped with boron and 1% (w/w) magnesium were presented in Figure 5.10. It was seen that the major absorbance at wavelengths less than 400 nm was pertaining to the intrinsic band gap absorption of titanium dioxide (3.2 eV). The boron doped samples all exhibit red shifts in the band gap transition and the absorption edge in the spectrum of sample with 2% (w/w) boron and 1% (w/w) magnesium has the highest absorption. In addition, the boron doped samples also exhibit stronger absorption in the UV–vis range and 1% (w/w) Mg could be rised absorption spectra. The results of the absorption feature suggest that boron doped titanium dioxide could be activated by visible light and might exhibit enhanced photoresponse under UV light as well.

The addition of boron gave rise to a new absorption appears at around 400 to 600 nm. The boron-titanium dioxide photocatalyst had narrow band gap, showed optical absorption and photocatalytic activity in the visible region. Boron was incorporated into the crystal structure of TiO_2, which could narrow the band gap of titanium dioxide (Qincai et al., 2008). As seen in Figure 5.10, these UV-vis results of addition boron and magnesium showed a slight red-shift and displayed stronger absorption in both UV and visible range in comparison with pure titanium dioxide.

For the comparation band gap as shown in Table 5.9, which the boron doping has the reduced band gap energy. Thus, the boron doping effect to the activated visible region.
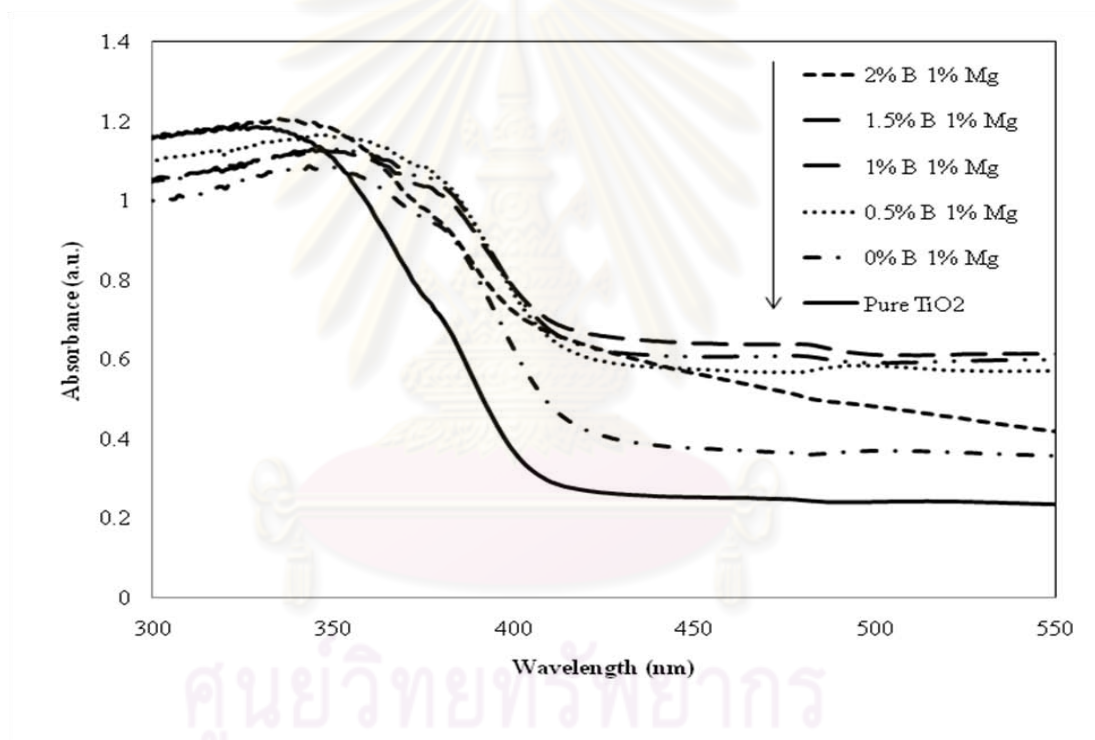
Figure 5.10 UV-visible absorption characteristics of titanium dioxide doped with various amount of boron and 1% (w/w) magnesium.

Table 5.9 The comparison band gap from UV-vis spectra of titanium dioxide doped with various amount of boron.

Catalyst	wavelength (nm)	band gap (eV)
pure TiO$_2$	421	2.95
0 (1% Mg)	440.58	2.81
0.5	449.95	2.76
1	455.84	2.72
1.5	461.4	2.69
2	464.91	2.67
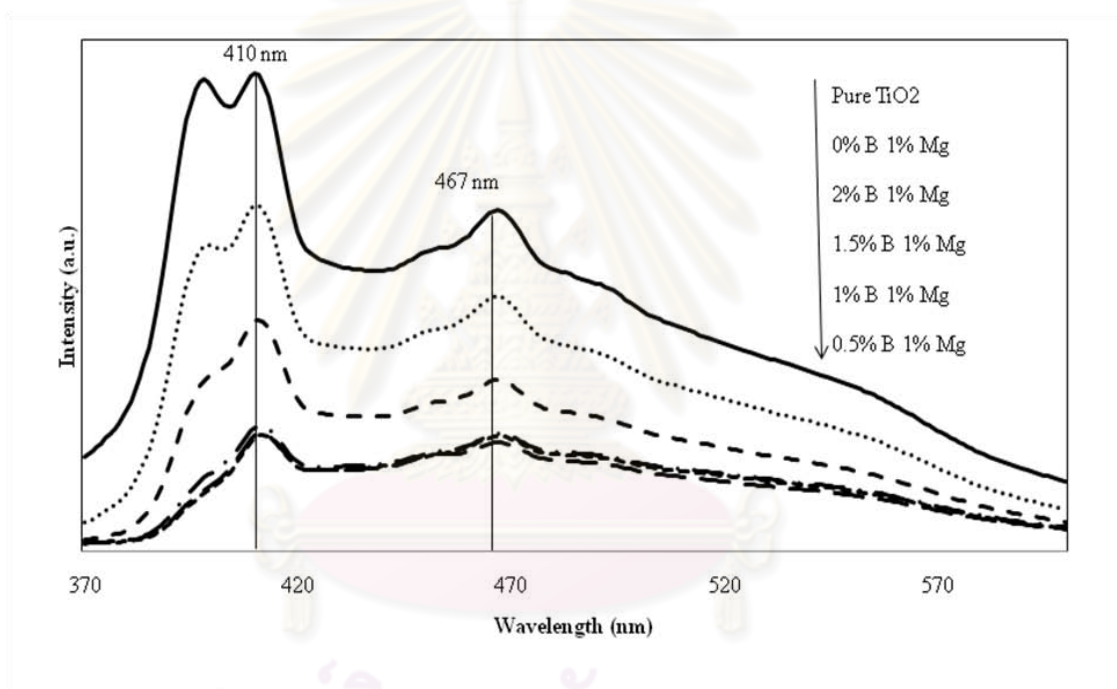
Figure 5.11 Photoluminescence emission signals in a range of 370-600 nm for titanium dioxide doped with various amount of boron and 1% (w/w) Mg.

5.2.5 Photoluminescence measurement

Photoluminescence emission spectrum was used to investigate the efficiency of charge carrier trapping, immigration, and transfer, and to understand the late of electrons and hole in titanium dioxide since photoluminescence emission resulted from the recombination of free carriers. Figures 5.11 displayed the photoluminescence spectra for the catalysts that were excited by irradiation with a wavelength of 350 nm at room temperature. Two main emission peaks were observed at wavelengths of 410 and 467 nm, which corresponded to band gap energies of 3.0 and 2.7 eV, respectively. The first emission peak was ascribed to the emission of band gap transition (or the recombination of photogenerated electrons and holes) at a wavelength of 410 nm. The second emission peak was ascribed to the emission signal originated from the energy levels of defects in the band gap, such as oxygen vacancies formed during sample preparation at a wavelength of 467 nm. The oxygen vacancies were generated because of partially incomplete crystallization. The variation in photoluminescence emission spectrum intensity resulted from the change of defect state on the shallow level of the titanium dioxide surface (Zhao et al., 2007). Figure 5.11 revealed that the photoluminescence signal of pure titanium dioxide was the highest among all the samples. Upon decreasing of boron (from 2% (w/w) to 0.5% (w/w)) with fixed 1% (w/w) magnesium, photoluminescence signals were decreased but only in range 0.5-1.5% (w/w) were no evident difference signal. It could be observed that the photoluminescence intensity of 0.5% (w/w) sample was significantly lower than the highest boron content or only 1% (w/w) magnesium doping (0% (w/w) B). This result indicated that the recombination of charge carriers was effectively suppressed after boron and magnesium doped on titanium dioxide. Oxygen vacancies are also involved in photo-catalysis on oxides, and their charged nature may control band-bending and thus electron-hole pair separation. But more oxygen vacancy defects may also become the recombination center. The existence of oxygen vacancies is in favor of the occurrence of dissociative adsorption, generating active free radicals and promoting the photo-catalytic reaction (Bai et al., 2010). Thus, it could be observed that the peak oxygen vacancies intensity of 2% (w/w) sample was significantly higher than the other boron content which might be the best photocatalytic activity.

5.2.6 X-ray photoelectron spectroscopy (XPS)

The XPS spectra for B/TiO_2 samples were recorded with photon energy of 1256 eV (Mg K_α). For all measurements, the kinetic energies of the emitted electrons in the range of 0-1000 eV were detected. Figure 5.12 a) and b) was showed the XPS spectra of 2% (w/w) B and 1% (w/w) Mg. Figure 5.12 a) revealed that the binding energy (BE) for B1s was 192 eV, 197.4 eV and 187.2 eV. Base on the previous researches reported in the literature, the binding energies for B1s were 193.6 eV in B_2O_3 (B-O bond), 193.0 eV in H_3BO_3 (B-O bond), and 187.5 eV in TiB_2 (Ti-B bond). One peak, around 192 eV, could be attributed to the B-O-Ti bond. At some peak 187.5 eV and 197.4 eV, indicated that the some boron atoms were bonded by means of B-Ti-B bond or B-O bond. From figure 5.12b, it could be observed for Mg2p was 52.9 eV, 48.9 eV and 50.9 eV. According to the report, the BE for Mg2p in MgO was 51.21 eV. The experimental results of XPS concluded that the entry of Mg^{2+} ion into TiO_2 lattice is substitutional, which is typical of Mg^{2+} that bonds with oxygen atom.

5.2.7 Fourier transform infrared spectroscopy (FT-IR)

The FT-IR spectra of $B-Mg-TiO_2$ samples fired at 350ºC are shown in Figure 5.13, several peaks at 500-4000 cm^{-1} were observed the peaks of C–O bond at 1026 cm^{-1}, C–O–C bond at 1224 cm^{-1}, C–OH bond at 1370 cm^{-1}, C=O bond at 1740 cm^{-1}, C=C bond at around 1636 cm^{-1}, and a broad peak at the range of 3000–3500 cm^{-1} which is attributed to the O–H stretching vibrations of the C–OH groups and water. The peak at 2336 cm^{-1} can be assigned to the absorption peak of carbon dioxide (CO_2), which is attributed to the (C-C) stretching. Meanwhile, for all doped TiO_2 samples and Pure TiO_2, the broad absorption at low wave numbers (below 1000 cm^{-1}) is attributed to the vibration of Ti–O–Ti bonds in TiO_2 (Yupeng et al., 2011).

Table 5.10 was shown the peak height of C-C bond of boron and magnesium doping was calculated from FT-IR spectra, which varied from 1.1 to 26.4. The best peak height C-C bond as 1% (w/w) B and 1% (w/w) Mg were 26.4. Visible light activity could be enhanced by presence of carbonaceous species (C–C) occurred in highly condensed and coke-like structure, which could play the role of photosensitizer to induce the visible light absorption and response. Some carbon compounds existed

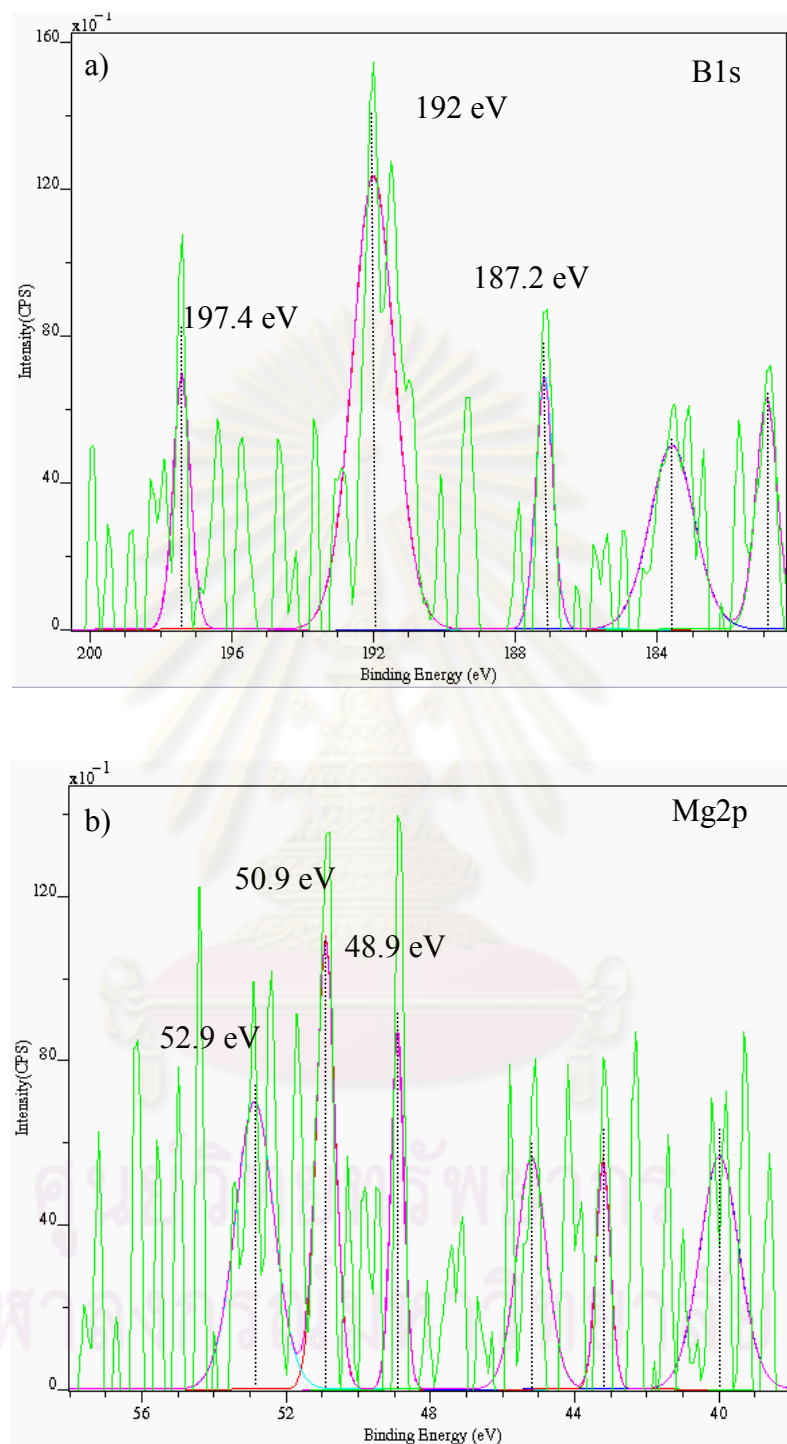at the photocatalyst, which might be from the precursor of titanium or adsorbed CO_2 in the air.

Figure 5.12 XPS spectrum of TiO_2 that was doped with 2% (w/w) B and 1% (w/w) Mg : a) B1s, b) Mg2p
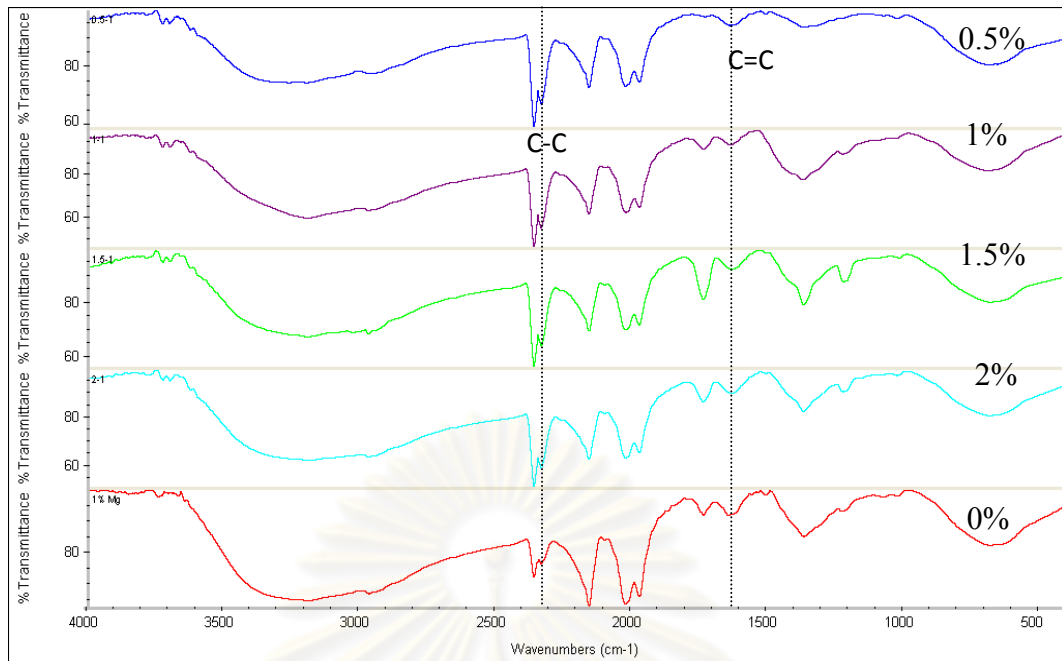
Figure 5.13 FTIR spectra for the boron and 1% (w/w) magnesium doped sample

5.2.8 Scanning electron microscope with energy-dispersive x-ray analyzing system (SEM-EDX)

As shown in Figure 5.14 a) and b), was analyzed the amount element of sample TiO_2 and boron doped TiO_2, respectively, as C, O, Mg, and Ti but not show peak the blinding energy (B_E) of B because the B_E value of B was lower than C that could not show the B peak by SEM-EDX. Table 5.11 was shown the different percent of each element in pure TiO_2 and boron doped TiO_2 sample, which was indicated that the amount of carbon in 1% (w/w) B 1% (w/w) Mg was higher than 2% (w/w) B 1% (w/w) Mg and pure TiO_2, agreement with FTIR spectra that was shown the carbonaceous species act as a photosensitiser.

Table 5.10 Calcution peak height(C-C) from FTIR spectra for the boron and 1% (w/w) magnesium doped sample.

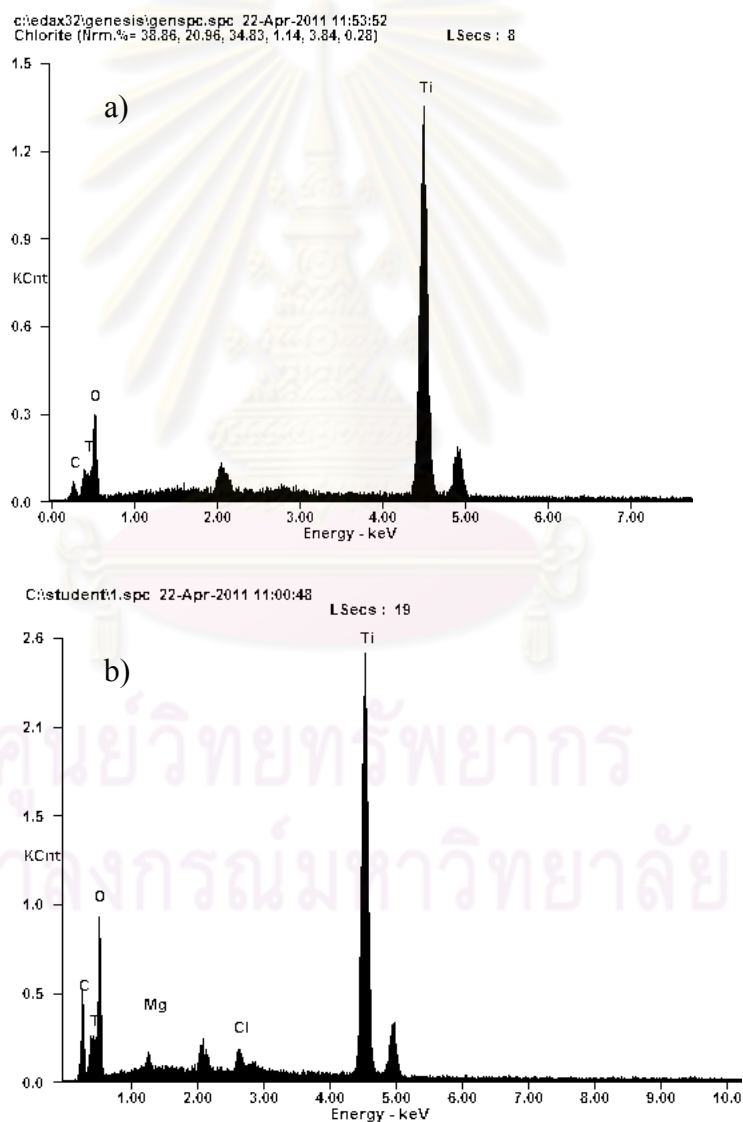| B doping (% (w/w))	height (C-C)
Pure TiO$_2$	1.131
0(1% Mg)	7.4920
0.5	23.0780
1	26.3530
1.5	22.5160
2	21.7520

Figure 5.14 SEM-EDX analysis for determine the percent of element the boron and magnesium doped sample : a) Pure TiO$_2$, b) 1% (w/w) B 1% (w/w) Mg

Table 5.11 Calculation percent of element by SEM-EDX for the boron doped and magnesium sample

Element	C		O		Mg		Ti	
%(w/w)	wt%	at%	wt%	at%	wt%	at%	wt%	at%
0% B 1% Mg	2.41	5.05	40.84	64.40	1.28	1.33	55.47	29.22
1% B 1% Mg	11.66	24.47	26.85	42.31	1.04	1.07	58.71	30.90
2% B 1% Mg	4.39	9.09	39.20	60.89	1.48	1.52	54.93	28.50

5.2.9 Photocatalytic activity

- The reaction under UV light irradiation (200-400 nm)

Figure 5.15 showed the amount of hydrogen production from splitting water versus irradiation time under UV light illumination: B doped catalyst was fixed 1% (w/w) Mg, which was used to test the photocatalytic activity. One could observe that all boron-magnesium prepared samples exhibited more photocatalytic activity than pure titanium dioxide and only magnesium doping under UV light. It could be also seen that the addition of boron and magnesium sample had an effect on the decomposition of water. The order of decreasing activity was 2% (w/w) B, 1.5% (w/w) B, 1% (w/w) B, 0.5% (w/w) B, 0% (w/w) B and pure TiO_2. This result agreed with the result from UV-vis spectra in Figure 5.10.

The enhancement of photoactivity of TiO_2 has been demonstrated using dopant metal ions or oxides to modify the band gap or to act as charge separators of the photoinduced electron–hole pair. Venkatachalam and coworkers (2007) proposed the formation of Ti–O–Mg inhibits the transition of TiO_2 phase and prevents the agglomeration of TiO_2 nano particles and growth of rutile phase. Hence, the entry of Mg^{2+} ions into the TiO_2 lattices suppressed the particle growth and consequently increased the band gap value of nano TiO_2, which minimized the electron–hole recombination during the photocatalytic degradation of organic compounds.
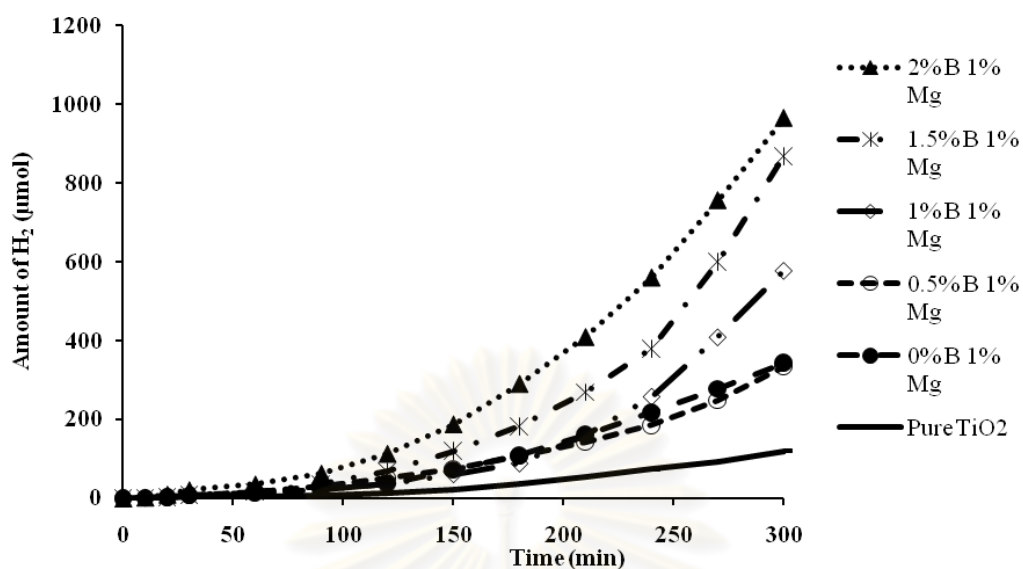
Figure 5.15 Amount of hydrogen produced from photocatalytic water splitting over titanium dioxide doped with various amount of B and 1% (w/w) Mg under UV light irradiation.
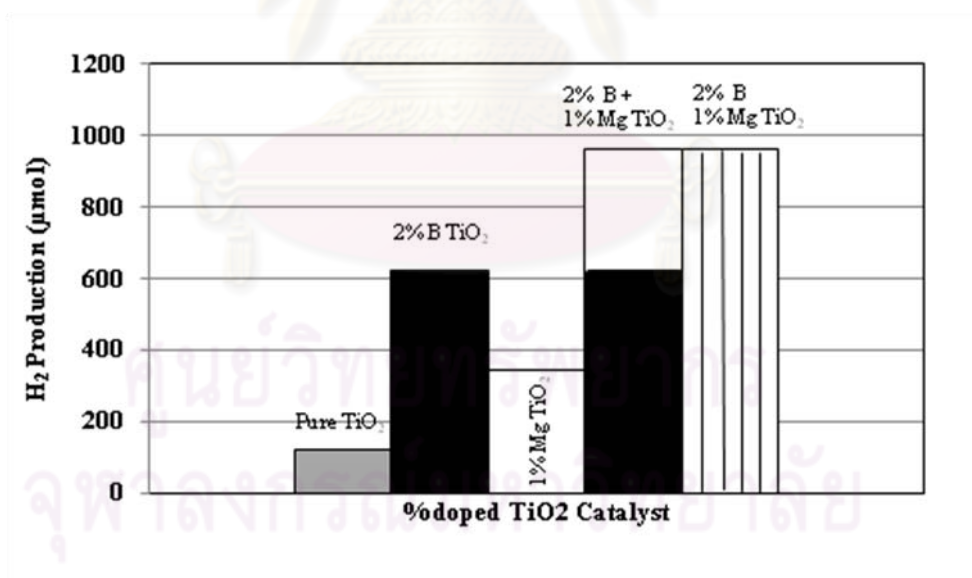

Figure 5.16 Amount of hydrogen produced by pure titanium dioxide doped and various amount of 2% (w/w) B and 1% (w/w) Mg under UV light irradiation, which compared by synergetic effect.

Among the samples, the best performance was attributed to 2% (w/w) B and 1% (w/w) Mg corresponding to the XPS results (see Figure 5.12). It could be calculated that the photocatalytic performance of 2% (w/w) B and 1% (w/w) Mg was almost 10 times higher than that of pure titanium dioxide for decomposition of water under UV light. Obviously, the photocatalytic activity of B-Mg doped TiO_2 under UV light demonstrated that B doping effect was outstanding with amount of hydrogen more than undoped TiO_2. This was ascribed to the cooperative effects of B and Mg doping. These agreed with the outcome from the UV-vis absorption spectra and photoluminescence analysis.

Figure 5.16 compared the amount of hydrogen gas that was produced by photocatalytic water splitting over pure TiO_2, TiO_2 doped with only 2% (w/w) B, TiO_2 doped with only 1% (w/w) Mg, and TiO_2 doped with 2% (w/w) B and 1% (w/w) Mg after 300 minutes of reaction times. The amount of hydrogen produced from TiO_2 doped with both B and Mg was significant equability with the sum of the amount of hydrogen produced from TiO_2 that was doped B with Mg which might be revealed that the doping TiO_2 had synergetic effect.

- The reaction under visible light irradiation (400-700 nm)

Figure 5.17 showed the amount of hydrogen production from splitting water versus irradiation time under visible light illumination: B doped catalyst was fixed 1% (w/w) Mg, which was used to test the photocatalytic activity. One could observe that all boron-magnesium prepared samples exhibited more photocatalytic activity than pure titanium dioxide under visible light. It could be also seen that the addition of boron sample had an effect on the decomposition of water. The orders of decreasing activity were 1% (w/w), 1.5% (w/w), 0.5% (w/w), 2% (w/w) B, 0% (w/w) B and pure TiO_2 and some samples were the same as the order of increasing UV-vis spectra (see Figure 5.10). It observed that 2% (w/w) B had lowest characteristic of UV-vis spectra and photoluminescence measurement, effect to lowest activity when compared with other doped samples. Only 1% (w/w) B was not agreed with characteristic analysis which 1% (w/w) B had seem the characteristic of range 0.5-1% (w/w) B, in UV-vis and photoluminescence measurement but evidence highest activity. Both carbon and boron showed beneficial influence on the photodegradation efficiency in visible light activity (Zaleska et al., 2008).

However, photoactivity under visible light of all samples could originate from both carbon and boron presence, see from FT-IR result (Figure 5.13), regarding the role of carbon as a photosensitiser of C-C bond (photosensitiser references Page 43). These FT-IR results in Table 5.10, could be listed as follows: 1% (w/w) B > 1.5% (w/w) B > 0.5% (w/w) B > 2% (w/w) B, agreed with photocatalytic activity and more than only boron doped.

As shown in Figure 5.17, the visible light induced H_2 production was remarkably enhanced by doping TiO_2 with B. Sample of 1% (w/w) B 1% (w/w) Mg exhibits the highest activity with a hydrogen production rate as about 6 times of pure titanium dioxide for decomposition of water under visible light.

According to Bandara and coworkers (2004) proposed that the enhanced photocatalytic activity of TiO_2/MgO is explained as resulting from the high probability of trapping of an excited electron in the CB of TiO_2 by attached MgO and holes remain in the valence band (VB) of TiO_2. This process leads to efficient spatial separation of photogenerated charges (e^- and h^+) suppressing recombinations, leading to higher photoactivities and the plausible mechanism is presented. Our results were also in good agreement with them.

Figure 5.18 compared the amount of hydrogen gas that was produced by photocatalytic water splitting over pure TiO_2, TiO_2 doped with only 1% (w/w) B, TiO_2 doped with only 1% (w/w) Mg, and TiO_2 doped with 1% (w/w) B and 1% (w/w) Mg after 300 minutes of reaction times. The amount of hydrogen produced from TiO_2 doped with both B and Mg was significantly higher than the sum of the amount of hydrogen produced from TiO_2 that was doped B with Mg which could revealed that the doping TiO_2 had synergetic effect.

From Figure 5.16 and 5.18 found that the photocatalytic activity under visible light was observed higher photocatalytic activity than under UV light irradiation. Wendong and coworkers (2005) proposed that the synergetic effect could be explained in terms of carbon role as photosensitizer, especially visible region which it can induced visible light region. The PL and SEM-EDX spectra (Figure 5.11) result were observed that 1% (w/w) B with 1% (w/w) Mg has the highest carbon content. Thus, the photocatalytic activity under visible light irradiation was clearly observed than UV light irradiation. The doping B and Mg lead to more active catalyst under visible light due to the reduced band gap.
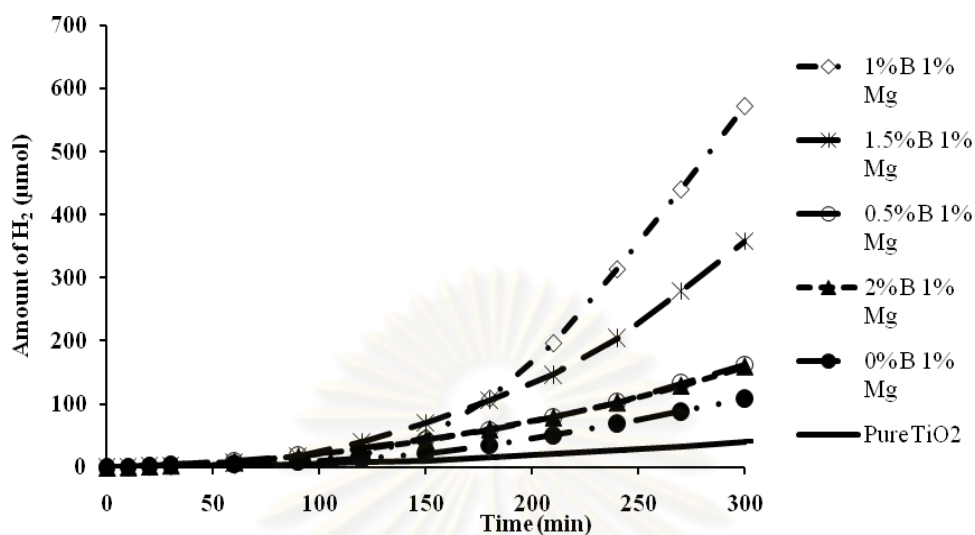
Figure 5.17 Amount of hydrogen produced from photocatalytic water splitting over titanium dioxide doped with various amount of B and 1% (w/w) Mg under day light irradiation.
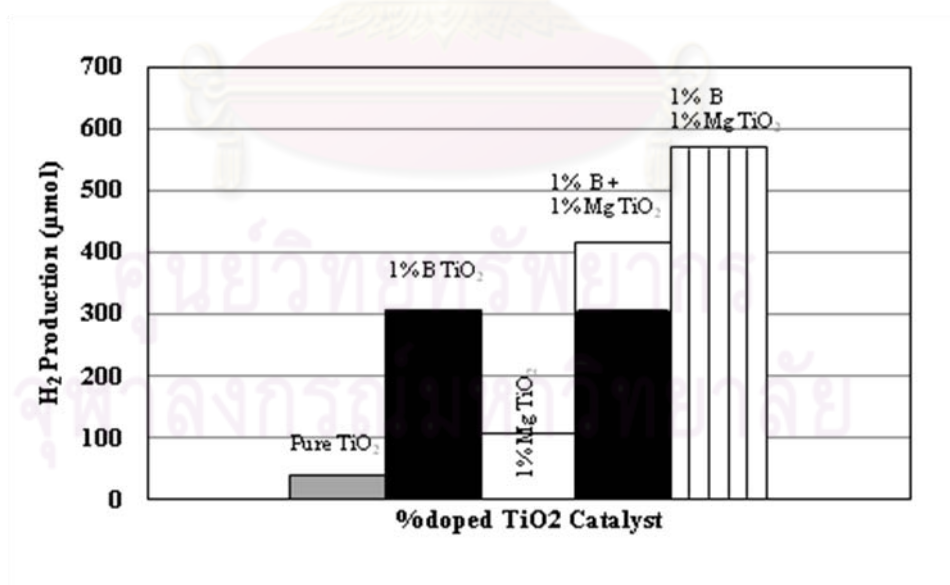

Figure 5.18 Amount of hydrogen produced by pure titanium dioxide doped and various amount of 1% (w/w) B and 1% (w/w) Mg under day light irradiation, which compared by synergetic effect.

Table 5.12 was explained the synergetic effect of catalyst in the photocatalytic activity for UV and visible light. For 1% (w/w) B 1% (w/w) Mg, the carbon content was higher than the combination of 1% (w/w) B and 1% (w/w) Mg. The higher carbon content results in the increasing of photocatalytic activity under visible light. For 2% (w/w) B 1% (w/w) Mg, the carbon content was lower than the combination of 2% (w/w) B and 1% (w/w) Mg, which not significantly increased the photocatalytic activity under UV light. Some carbon compounds existed at the photocatalyst, which might be from the precursor of titanium and heating procedure.

Table 5.12 The relative of carbon content and photocatalytic activity

% (w/w) Doped TiO$_2$	C content (%wt.)	Hydrogen production in UV light (μmole)	Hydrogen production in visible light (μmole)
Pure TiO$_2$	2.09	120.3	40.3
0% B 1% Mg	2.41	344.2	108.3
1% B	2.77	400.4	306.2
1% B + 1% Mg	5.18	744.6	414.5
1% B 1% Mg	11.66	578.1	571.9
2% B	2.70	621.3	45.2
2% B + 1% Mg	5.11	965.5	153.5
2% B 1% Mg	4.39	964.2	159.0

CHAPTER VI

CONCLUSIONS AND RECOMMENDATIONS

6.1. Conclusions

Photocatalytic activity of titanium dioxide for water splitting was enhanced by addition of B. The highest activity under UV irradiation was observed in titanium dioxide doped with 2% (w/w) B. To improve the activity further, Boron was doped to TiO_2 together with either Mg which 2% (w/w) B and 1% (w/w) Mg had the highest activity under UV irradiation. The photocatalytic activity of co-doped TiO_2 increased under UV irradiation as the boron loading increased because of better absorption in the visible region and slower recombination of photogenerated charge carriers. The addition of boron or magnesium to TiO_2 has supposed to increase the hydrogen production, reduced recombination of the holes and back transferred electrons. Consequently, the efficiency of doping with titanium dioxide photocatalytic have higher than that of the photocatalyst contained pure TiO_2, when irradiation by UV range. In contrast for day light irradiation, 1% (w/w) B and 1% (w/w) Mg was the best photocatalyst due to carbonaceous species plays the role of photosensitiser.

6.2. Recommendations for future studies

1. In this work, the some doping sample was fixed 1% (w/w) Mg, which had an effect on its photocatalytic activity. Therefore, one may vary the amount of magnesium doping.

2. This research was recovered about irradiation both UV and visible irradiation had suitable effective for boron and magnesium doping. Hence, the application with solar light should be investigated.

3. Other boron precursors should be used in the catalyst preparation step, which it can affect to photocatalytic activity in degradation of chemical.

4. From the drawback of photocatalytic water splitting technology about H_2-O_2 separation should be used photoelectrolysis by electricity input together with selective membrane that it can select only generated electron through the membrane for producing hydrogen production.

REFERENCES

Arai, N., Saito, N., Nishiyama, H., Domen, K., Kobayashi, H., Sato, K., and Inoue, Y. Effects of divalent metal ion (Mg^{2+}, Zn^{2+} and Be^{2+}) doping on photocatalytic activity of ruthenium oxide-loaded gallium nitride for water splitting. Catalysis Today 129 (2007): 407–413.

Adriana, Z., Janusz W. S., Ewelina, G., and Jan, H. Preparation and photocatalytic activity of boron-modified TiO_2 under UV and visible light. Applied Catalysis B: Environmental 78 (2008): 92–100.

Adriana, Z., Ewelina, G., Janusz, W.S., Maria, G., and Jan, H. Photocatalytic activity of boron-modified TiO_2 under visible light: The effect of boron content, calcination temperature and TiO_2 matrix. Applied Catalysis B: Environmental 89 (2009): 469–475.

Bandara, J.C., Hadapangoda, C., and Jayasekera, W.G. TiO_2/MgO composite photocatalyst: the role of MgO in photoinduced charge carrier separation. Applied Catalysis B: Environmental 50 (2004): 83–88.

Bai, A., Liang, W., Zheng, G., and Xue, J. Preparation and Enhanced Daylight-Induced Photo-Catalytic Activity of Transparent C-Doped TiO2 Thin Films. Journal of Wuhan University of Technology-Material Science 25 (2010): 738-742

Chen, J.N., Chan, Y.C., and Lu, M.C. Photocatalytic oxidation of chlorophenols in the presence of manganese ions. Water Science and Technology 39 (1999): 225–230.

Chetpaisalsakul, W. Effect of surface defect of titanium dioxide on photocatalytic for water decomposition to hydrogen. Chulalongkorn University (2006).

Christian, L., Knut H., Horst, K., Macyk, W., and Wilhelm, F. M. Visible light photodegradation of 4-chlorophenol with a coke-containing titanium dioxide photocatalyst. Applied Catalysis B: Environmental 32 (2001): 215–227

Eakachai, M. Bimetallic doping of titanium dioxide for use in photocatalytic splitting of water. Chulalongkorn University (2007)

Francisco, M.S.P., and Mastelaro, V.R. Inhibition of the anatase-rutile phase transformation with addition of CeO_2 to $CuO-TiO_2$ system: Raman spectroscopy, X-ray diffraction, and textural studies. Chemistry Material. 14 (2002): 2514.

Grabowska, E., Zaleska, A., Sobczak, J.W., Gazdac, M., and Hupkaa, J. Boron-doped TiO_2: Characteristics and photoactivity under visible light. Procedia Chemistry 1 (2009): 1553–1559.

Guo, L.J., Zhao, L., Jing, D.W., Lu, Y.J., Yang, H.H., Bai, B.F., Zhang, X.M., Ma, L.J., and Wu, X.M. Solar hydrogen production and its development in China. Energy 34 (2009): 1073–1090

Hwang, D.W., Kim, J., Park, T.J., and Lee, J.S. Mg-doped WO_3 as a novel photocatalyst for visible light-induced water splitting. Catalysis Letters Vol.80 Nos.1-2 (2002): 53-57.

Khana, R., Kim, S., Kim, T-J., and Nam, C-M. Comparative study of the photocatalytic performance of boron-iron co-doped and boron-doped TiO_2 nanoparticles. Materials Chemistry and Physics 112 (2008): 167‑172.

Kudo, A. Development of photocatalyst materials for water splitting. International Journal of Hydrogen Energy 31 (2006): 197–202.

Liu, Y., Guo, L., Yan, W., and Liu, H. A composite visible-light photocatalyst for hydrogen production. Journal of Power Sources 159 (2006): 1300–1304.

Marta, I-L. Review heterogeneous photocatalysis transition metal ions in photocatalytic systems. Applied Catalysis B: Environmental 23 (1999): 89–114.

Moon, S-C., Mametsuka, H., Tabata, S., and Suzuki, E. Photocatalytic production of hydrogen from water using TiO_2 and B/TiO_2. Catalysis Today 58 (2000): 125–132.

Meng, N., Michael, K.H.L., Dennis, Y.C., and Leung, K. Sumathy. A review and recent developments in photocatalytic water-splitting using TiO_2 for hydrogen production. Renewable and Sustainable Energy Reviews 11 (2007): 401–425.

Na, L., Huimin, Z., Jingyuan, L., Xie, Q., and Shuo, C. Characterization of boron-doped TiO_2 nanotube arrays prepared by electrochemical method and its visible light activity. Separation and Purification Technology 62 (2008): 668–673.

Qincai, L., Jianzhong, S., and Qiyun, Z. Preparation and characterization of visible-light-driven titania photocatalyst co-doped with boron and nitrogen. Applied Surface Science 254 (2008): 3236–3241.

Qincai, L., Jianzhong, S., Qiyun, Z., Qian, Z., and Hua, R. Visible-light-driven titania/silica photocatalyst co-doped with boron and ferrum. Applied Surface Science 254 (2008): 6731–6735.

Su, C. , Hong, B.-Y., and Tseng, C.-M. Sol–gel preparation and photocatalysis of titanium dioxide. Catalysis Today 96 (2004): 119–126.

Tryba, B., Tsumura, T., Janus, M., Morawski, A.W., and Inagaki, M. Carbon-coated anatase: adsorption and decomposition of phenol in water. Applied Catalysis B: Environmental 50 (2004): 177–183.

Venkatachalam, N., Palanichamy, M., and Murugesan, V. Sol–gel preparation and characterization of alkaline earth metal doped nano TiO_2: Efficient photocatalytic degradation of 4-chlorophenol. Journal of Molecular Catalysis A: Chemical 273 (2007): 177–185.

Wu, N-L., Lee, M-S., Pon, Z-J., and Hsu, J.-Z. Effect of calcination atmosphere on TiO_2 photocatalysis in hydrogen production from methanol/water solution. Journal of Photochemistry and Photobiology A: Chemistry 163 (2004): 277–280.

Wendong, W., Philippe, S., Philippe, K., and Joaquim, L. F. Visible light photodegradation of phenol on MWNT-TiO2 composite catalysts prepared by a modified sol–gel method. Journal of Molecular Catalysis A: Chemical 235 (2005): 194–199

Yuexiang, L. , peng, S. , Jiang, F. , Lu, G., and Li, S. Effect of doping TiO_2 with alkaline-earth metal ions on its photocatalytic activity. Journal of the Serbian Chemical Society 72 (4) (2007): 393–402.

Yuexiang, L., Ma, G. , Peng, S. , Lu, G., and Li, S. Boron and nitrogen co-doped titania with enhanced visible-light photocatalytic activity for hydrogen evolution. Applied Surface Science 254 (2008): 6831–6836.

Yaling, S., Song, H., Xingwang, Z., Xiuqin, C., and Lecheng, L. Preparation and visible-light-driven photoelectrocatalytic properties of boron-doped TiO2 nanotubes. Materials Chemistry and Physics 110 (2008): 239–246

Yupeng, Z., and Chunxu, P. TiO2/graphene composite from thermal reaction of grapheme oxide and its photocatalytic activity in visible light. <u>Journal of Material Science</u> 46 (2011): 2622–2626

Zhao, Y., Chunzhong, L., Xiuhong, L., Feng, G., Haibo, J., Wei, S., Ling, Z., and Ying, H. Synthesis and optical properties of TiO_2 nanoparticles. <u>Materials Letters</u> 61 (2007): 79–83.

Zhimang, S., Baozhu, T., and Jinlong, Z. Enhanced photocatalytic activity of mesoporous TiO_2 with MgO coating. <u>Materials Letters</u> 63 (2009): 1705–1708.

ศูนย์วิทยทรัพยากร
จุฬาลงกรณ์มหาวิทยาลัย

APPENDICES

APPENDIX A

CALCULATION FOR CATALYST PREPARATION

Calculation for the amount of boron precursor to be used during the incipient wetness impregnation method is shown below.

Reagent: - Boric acid (H_3BO_3) Molecular weight =   61.83 g/mol

- Magnesium chloride ($MgCl.6H_2O$) = 203.3 g/mol

-Support: Titania [TiO_2]

Example Calculation for the preparation of 2% (w/w) B on TiO_2

Based on 100 g of catalyst used, the composition of the catalyst is

    Boron   =   2 g

    Titania   =   100-2   =   98 g

For 5 g of titania

Boron required   =   5 x (2/98)   =   0.1020 g

Boron 0.1020 g was prepared from H_3BO_3 and molecular weight of B is 10.811 g/mol

$$H_3BO_3 \text{ required} = \frac{\text{MW of } H_3BO_3 \times \text{Boron required}}{\text{MW of B}}$$

$$= (61.83/10.811)\text{x}0.1020 = 0.5834 \text{ g}$$

Calculation for the preparation of 1% (w/w) Mg on TiO_2

Based on 100 g of catalyst used, the composition of the catalyst is

    Magnesium   =   1 g

    Titania   =   100-1   =   99 g

For 5 g of titania

Magnesium required   =   5 x (1/99)   =   0.0505 g

Magnesium 0.0505 g was prepared from $MgCl.6H_2O$ and molecular weight of Mg is 24.305 g/mol

$MgCl.6H_2O$ required $= \dfrac{\text{MW of } MgCl.6H_2O \times \text{Magnesium required}}{\text{MW of Mg}}$

$= (203.3/24.305) \times 0.0505 \qquad = \qquad 0.4224$ g

APPENDIX B

CALCULATION OF THE CRYSTALLITE SIZE

Calculation of the crystallite size by Debye-Scherrer equation

The crystallite size is calculated from the half-height width of the diffraction peak of XRD pattern using the Debye-Scherrer equation.

From Scherrer equation:

$$D = \frac{K\lambda}{\beta \cos\theta}$$

(A.1)

Where   D = Crystallite size, Å

K = Crystallite-shape factor = 0.9

λ = X-ray wavelength, 1.5418 Å for CuKα

θ = Observed peak angle, degree

β = X-ray diffraction broadening, radian

The X-ray diffraction broadening (β) is the pure width of a powder diffraction free of all broadening due to the experimental equipment. Standard α-alumina is used to observe the instrumental broadening since its crystallite size is larger than 2000 Å. The X-ray diffraction broadendening (β) can be obtained by using Warren's formula.

From Warren's formula:

$$\beta^2 = B_M^2 - B_S^2$$

(A.2)

$$\beta = \sqrt{B_M^2 - B_S^2}$$

Where B_M = The measured peak width in radians at half peak height.

B_S = The corresponding width of a standard material.

Example: Calculation of the crystallite size of titanium dioxide

The half-height width of 101 diffraction peak $=$ 1.7395 $^{\circ}$

$=$ 0.0303 radian

The corresponding half-height width of peak of α-alumina $=$ 0.0038 radian

The pure width $=$ $\sqrt{B_M^2 - B_S^2}$

$=$ $\sqrt{0.0303^2 - 0.0038^2}$

$=$ 0.0301 radian

β $=$ 0.0301 radian

2θ $=$ 25.55 $^{\circ}$

θ $=$ 12.78 $^{\circ}$

λ $=$ 1.5418 Å

The crystallite size $=$ $\dfrac{0.9 \times 1.5418}{0.0301\cos 12.78}$ $=$ 47.27 Å
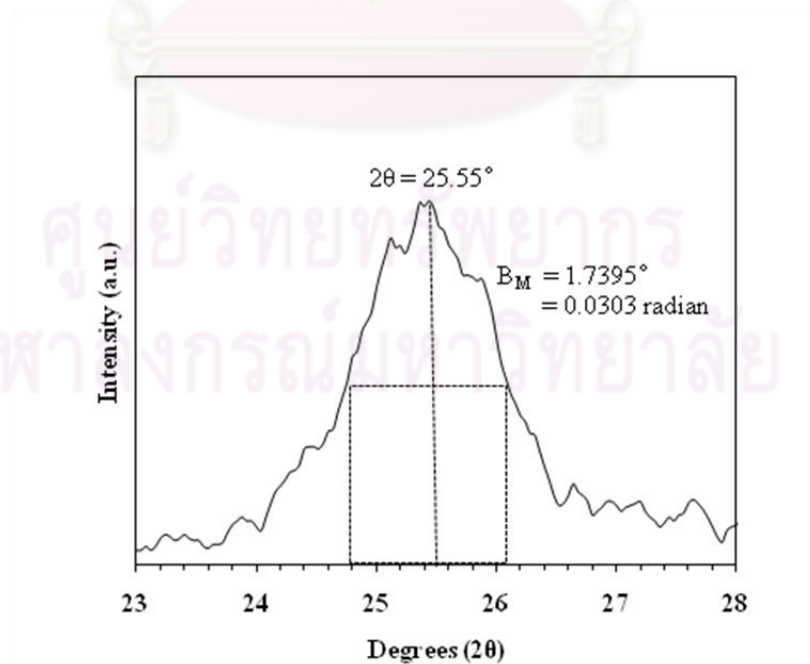
$=$ 4.73 nm

Figure B.1 The 101 diffraction peak of titanium dioxide for calculation of the crystallite size

APPENDIX C

CALIBRATION CURVES

This appendix presented the calibration curve for calculation of products in photocatalytic reaction of water decomposition to hydrogen.

The thermal conductivity detector, gas chromatography Shimadza model 8A was used to analyse the concentration of hydrogen by using Molecular sieve 5A column. The operating conditions for each instrument were described in the section 4.3.

Mole of hydrogen in y-axis and area reported by gas chromatography in x-axis are exhibited in the curves. The calibration curve of hydrogen is illustrated in the following Figure C.1.
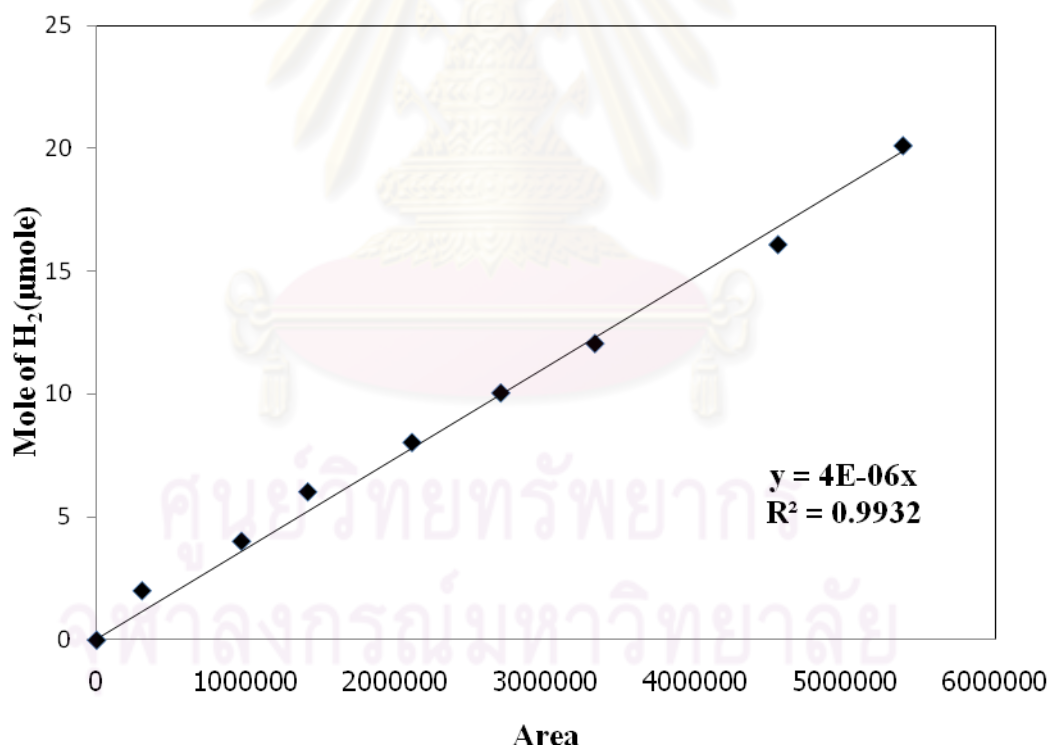

Figure C.1 The calibration curve of hydrogen

APPENDIX D

ELECTRON SPIN RESONANCE SPECTROSCOPY

Electron spin resonance spectroscopy (ESR) was performed to determine the amount of Ti^{3+} defects in the catalyst. Typical result was displayed in Figure D.1. The peak observed at the g value of 1.997 was assigned to Ti^{3+} defects. The peak height was proportional to the amount of Ti^{3+} in the catalyst. The modification of titanium dioxide surface states can increased the photocatalytic activity and was explained by the increase in Ti^{3+} surface defects of modified titanium dioxide (Waraporn, 2006). Hence, based on this present study, the roles of surface defects (Ti^{3+}) sites on this photocatalytic reaction can be proposed that it acted as trapping photoelectron sites. This suggests that the more there are Ti^{3+} on the surface of titanium dioxide, the better the photocatalytic activity value. Some ESR peak signals (broad peak) at 1.5% (w/w) and 2% (w/w) B, were not clearly observed at the g value of 1.997. It could not reference with theory data. This ESR result was not agreed with the order of B doping and photocatalytic activity.
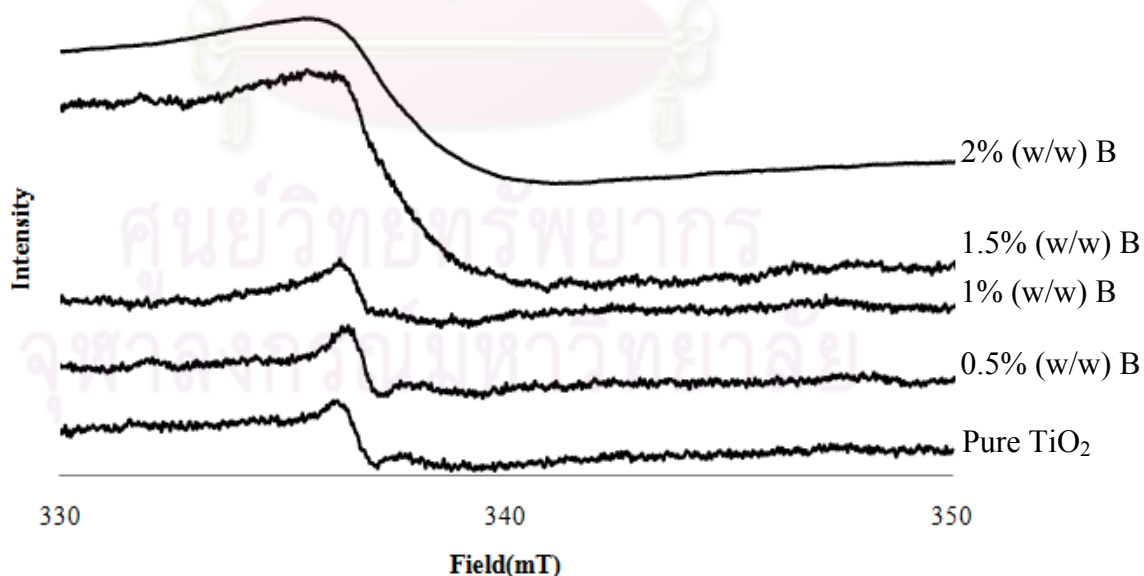

Figure D.1 Peak height ESR results of titanium dioxide doped with various amount of boron.

In Figure D.2, Some ESR peak signal (broad peak) at 0.5% (w/w) B was not clearly observed at the g value of 1.997. It could not reference with theory data. This ESR result was not agreed with the order of B-Mg doping and photocatalytic activity.
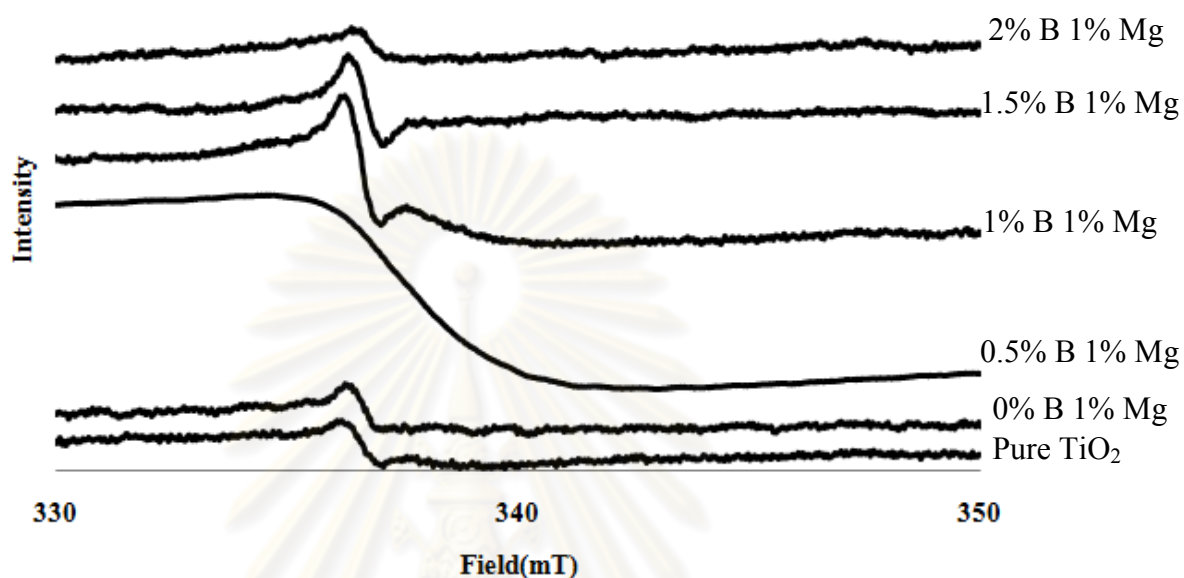

Figure D.2 Peak height ESR results of titanium dioxide doped with various amount

of B and 1% (w/w) Mg.

APPENDIX E

THE CALCULATION OF THE BAND GAP FROM UV-VIS SPECTRA

The band gap (E_g) of the sample was determined by the following equation (Eq.1):

$$E_g = \frac{1240}{\lambda}$$

(Eq.1)

Where E_g is the band gap (eV) of the sample, λ (nm) is the wavelength of the onset of the spectrum.

The linear equation of Titanium dioxide line: $y = -0.0175x + 7.3676$; $R^2 = 0.9978$

$E_g = y = 0$, λ (nm) $= x = ?$

Solve linear equation and the λ (nm) of TiO_2 answer was: 421 nm

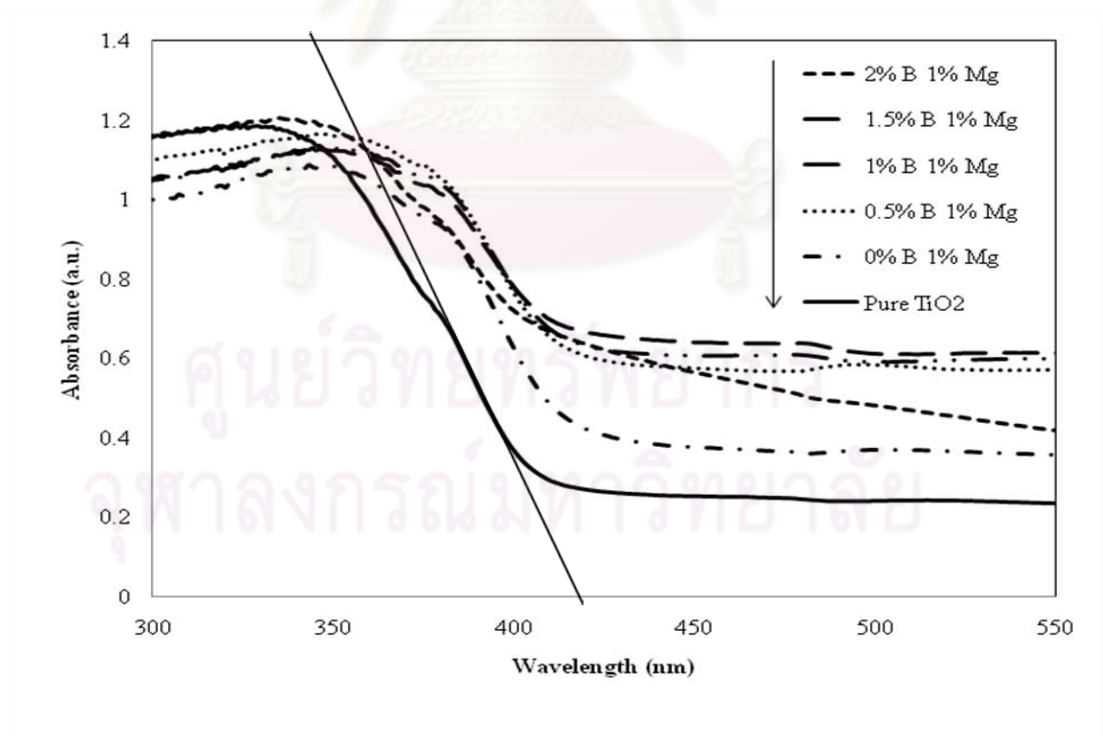Substitute λ in Eq.1; $E_g = 2.95$ eV

Figure E.1 UV-visible absorption characteristics of titanium dioxide doped with

various amount of boron and 1% (w/w) magnesium.

VITA

Ms. Chutinan Orak was born on June 24, 1987 in Chonburi, Thailand. She received the Bachelor Degree of Chemical Engineering from Faculty of Engineering, Prince of Songkhla University in 2009. She continued her Master's study at Chulalongkorn University in June, 2009.

Chutinan Orak, Akawat Sirisuk. "PHOTOCATALYTIC SPLITTING OF WATER OVER TITANIA DOPED WITH B AND Mg", Pure and Applied Chemistry International Conference 2011, Bangkok, Thailand, January 5-7, 2011.